Editors' Suggestion

Degenerate Parametric Amplification via Three-Wave Mixing Using Kinetic Inductance

Daniel J. Parker,[1] Mykhailo Savytskyi,[1] Wyatt Vine,[1] Arne Laucht,[1] Timothy Duty,[2] Andrea Morello,[1] Arne L. Grimsmo,[3] and Jarryd J. Pla[1,*]

[1] *School of Electrical Engineering and Telecommunications, UNSW Sydney, Sydney NSW 2052, Australia*
[2] *School of Physics, UNSW Sydney, Sydney, NSW 2052, Australia*
[3] *Centre for Engineered Quantum Systems, School of Physics, The University of Sydney, Sydney NSW 2006, Australia*

(Received 25 August 2021; revised 29 November 2021; accepted 17 February 2022; published 25 March 2022)

Degenerate parametric amplifiers (DPAs) exhibit the unique property of phase-sensitive gain and can be used to noiselessly amplify small signals or squeeze field fluctuations beneath the vacuum level. In the microwave domain, these amplifiers have been utilized to measure qubits in elementary quantum processors, search for dark matter, facilitate high-sensitivity spin resonance spectroscopy and have even been proposed as the building blocks for a measurement-based quantum computer. Until now, microwave DPAs have almost exclusively been made from nonlinear Josephson junctions, which exhibit high-order nonlinearities that limit their dynamic range and squeezing potential. In this work we investigate a microwave DPA that exploits a nonlinearity engineered from kinetic inductance. The device has a simple design and displays a dynamic range that is four orders of magnitude greater than state-of-the-art Josephson DPAs. We measure phase-sensitive gains up to 50 dB and determine that the device likely operates near the quantum noise limit. Additionally, we show that the higher-order nonlinearities that limit other microwave DPAs are almost nonexistent for this amplifier, which allows us to demonstrate its potential to perform squeezing by measuring the deamplification of coherent states by as much as 26 dB.

DOI: 10.1103/PhysRevApplied.17.034064

I. INTRODUCTION

High-performance cryogenic microwave amplifiers have become crucial components for an increasing number of contemporary experiments in condensed matter physics and quantum engineering. Microwave amplifiers that are based on parametric photon conversion are particularly promising since they can operate at the quantum noise limit, where only the minimal amount of noise required by quantum mechanics is added to the amplified signal. These amplifiers have facilitated the high-fidelity readout of quantum bits in elementary quantum processors [1], enabled spin resonance spectroscopy of femtoliter-volume samples [2] and are even aiding the search for axions [3,4].

Parametric amplifiers can be operated in one of two modes: phase insensitive or phase sensitive. In quantum mechanics, an electromagnetic field can be described by dimensionless quadrature field operators $I = (a^\dagger + a)/2$ and $Q = i(a^\dagger - a)/2$, where a and $a^\dagger$ are the boson annihilation and creation operators. In phase-insensitive amplification, gain G is applied equally to both quadratures, $\langle A\rangle = G\langle I\rangle$ and $\langle B\rangle = G\langle Q\rangle$ (where A and B represent the field at the output of the amplifier), unavoidably adding at least a quarter photon of noise to each quadrature in the process. Conversely, for phase-sensitive amplification, one field quadrature is amplified $\langle A\rangle = G\langle I\rangle$, while the other is deamplified, $\langle B\rangle = \langle Q\rangle/G$. This allows for amplification of a single quadrature without any added noise [5]. The noiseless nature of a phase-sensitive amplifier makes it distinctly useful for detecting small microwave signals, particularly those at the single-photon level [6].

In addition to its exceptional noise performance, a phase-sensitive amplifier can be used to reduce the fluctuations of an electromagnetic field. A mode of electromagnetic radiation cooled to its ground state will exhibit a quantum mechanical noise referred to as "vacuum fluctuations." These fluctuations obey the uncertainty relation $\delta I^2 \delta Q^2 \geq 1/16$, where δI^2 and δQ^2 represent the variances of the field quadratures (in dimensionless units of photons), and establish the ultimate limit to noise for measurements of an electromagnetic field. When a field in its quantum ground state enters a phase-sensitive amplifier, the vacuum fluctuations are deamplified or "squeezed" along one quadrature at the expense of increasing them along the other. Squeezed noise can be used to enhance the signal-to-noise ratio (SNR) in measurements and has

*jarryd@unsw.edu.au

been successfully deployed, for example, in gravitational wave detection [7].

In the microwave domain, the Josephson parametric amplifier (JPA) represents the state of the art in phase-sensitive amplification technology. A JPA consists of one or more Josephson junctions, typically in the form of a superconducting quantum interference device (SQUID), embedded in a low-quality-factor superconducting resonator [8,9]. Vacuum squeezing has been directly measured with JPAs employing single- cavity modes [so-called degenerate parametric amplifiers (DPAs)] at the level of 4.7 dB [3]. Higher levels of squeezing have been inferred (i.e., by removing the effects of loss and noise introduced by components after the JPA) both with single-cavity-mode JPAs (10 dB) [10] and devices that exploit entanglement of two distinct cavity modes (12 dB) [11]. However, recent experimental [12,13] and theoretical [14] investigations of JPAs have uncovered differences between the JPA and an ideal degenerate parametric amplifier, which become significant in the high gain limit (above 10 dB) and constrain the dynamic range and amount of inferred squeezing. Higher-order nonlinearities originating from the physics of Josephson junctions limit the useful linear regime of operation, with typical 1-dB compression points measuring less than −90 dBm at the amplifier output [15–17]. Attention has recently been focused on engineering JPAs with Hamiltonians that more closely resemble that of an ideal DPA, such as those employing junctions arranged in a superconducting nonlinear asymmetric inductive element (SNAIL) configuration [18–21], which has been successful in pushing 1- db-compression-point output powers to as high as −73 dBm.

In this work we present a phase-sensitive microwave parametric amplifier that behaves as a near-ideal DPA. The device contains no Josephson junctions (making it robust to electrostatic discharge) and is produced with a single-step lithography process on a thin film of niobium titanium nitride ($Nb_xTi_{1-x}N$). The nonlinearity responsible for parametric amplification in this device originates from a kinetic inductance intrinsic to the $Nb_xTi_{1-x}N$ film [22–27]. We observe up to 50 dB of phase-sensitive gain with a gain-bandwidth product of 53(7) MHz. An exceptionally large 1-dB-compression-point output power of −49.5(8) dBm is measured and represents an improvement of three to five order of magnitude over comparable JPAs.

We demonstrate that the weak nonlinearity of our amplifier also allows high levels of deamplification. This is achieved through mapping the phasor transformation of our DPA using coherent tones, where we observe deamplification levels approaching 30 dB without the distortions commonly observed in JPAs [12–14]. Although noise squeezing is not studied in this work, the deamplification levels reported represent an upper bound to the amount of vacuum squeezing that might be expected. Finally, we explore the noise properties of our amplifier and find that it likely operates close to the quantum noise limit.

II. THE KINETIC INDUCTANCE AMPLIFIER

Kinetic inductance is associated with the energy stored in the motion of charge-carrying particles. For superconducting films, Ginzburg-Landau theory predicts a current dependence of the kinetic inductance described by [28,29]

$$L_k(I) \approx L_0\left[1+\left(\frac{I}{I_*}\right)^2\right], \tag{1}$$

where L_0 is the per-unit-length kinetic inductance of the material without a current, and I_* determines the strength of the current dependence and is proportional to the critical current I_c of the film. This form of nonlinear inductance is analogous to an optical Kerr medium. When a current passing through the film consists of two different microwave tones [i.e., a signal tone (at a frequency ω_s) and a much stronger "pump" tone (at ω_p)], the nonlinearity gives rise to four-wave mixing (4WM), where energy transfer from the pump to the signal can produce parametric amplification [23,25]. In this process, two pump photons are converted to a signal photon and a photon at an additional tone called the "idler" (with frequency ω_i), where energy conservation requires $2\omega_p = \omega_s + \omega_i$. Introducing a dc current bias on top of the microwave tones, $I = I_{\rm dc} + I_{\mu w}$, lowers the order of the nonlinearity:

$$L_k(I) \approx L_0\left[1+\left(\frac{I_{\rm dc}}{I_*}\right)^2 + 2\frac{I_{\rm dc}I_{\mu w}}{I_*^2} + \left(\frac{I_{\mu w}}{I_*}\right)^2\right]. \tag{2}$$

In addition to the Kerr component (which is proportional to $I_{\mu w}^2$), a new term linear in $I_{\mu w}$ appears which can facilitate a three-wave mixing (3WM) process. Here a single pump photon produces a signal photon and an idler photon, such that $\omega_p = \omega_s + \omega_i$. Three-wave mixing is advantageous in the context of parametric amplification since there can be a large spectral separation between the pump and the signal. This means that the strong pump tone can be readily removed through filtering, preventing the saturation of any following amplifiers in the detection chain. Three-wave-mixing-type parametric amplifiers using kinetic inductance have been demonstrated recently in traveling-wave geometries [24,27]. However, at high pump powers a competition between 4WM and 3WM processes is known to degrade the parametric gain in devices and limit their performance [30]. In addition, there has been limited experimental work on phase-sensitive amplification in quantum-limited microwave traveling- wave devices.

Here we implement a resonant 3WM-type DPA that utilizes kinetic inductance and exhibits phase-sensitive gain. Critically, the resonant nature of our kinetic inductance parametric amplifier (KIPA) strongly suppresses 4WM and

other higher-order processes, permitting extremely high levels of pure 3WM gain. The device [see Fig. 1(a)] is fabricated in a 9.5-nm-thick film of niobium titanium nitride on silicon, benefiting from the high magnetic field resilience (up to $B_\perp \approx 350$ mT) and high critical temperature ($T_c \approx 10.5$ K) that are characteristic of this superconductor [31,32]. Niobium titanium nitride on silicon can exhibit extremely low losses with internal quality factors Q_i greater than 10^6 [33], which is advantageous for the generation of highly squeezed states and for performing amplification at the quantum noise limit. The amplifier is measured at a temperature of 20 mK in a dilution refrigerator (see Appendix B for experimental details).

The KIPA is defined geometrically by a coplanar waveguide (CPW) quarter-wavelength resonator (with resonant frequency ω_0) coupled to a single port via a microwave Bragg mirror [34,35], which can equivalently be viewed as a stepped-impedance band-stop filter [see Fig. 1(a)]. The filter is comprised of alternating sections of high-impedance ($Z_H = 126\ \Omega$) and low-impedance ($Z_L = 50\ \Omega$) CPW transmission line, each acting as a quarter-wavelength impedance transformer near the frequency ω_0. Their combined effect is to produce a large effective impedance $R_{\rm eff} = (Z_H/Z_L)^{2N} R_e$ (where $R_e = 50\ \Omega$ is the external impedance and N is the number of Z_H and Z_L repetitions) as seen by the quarter-wavelength resonator. The large $R_{\rm eff}$ creates a strong reflection and serves as the mirror for the single-port resonator. Importantly, the filter does not break the inner track of the CPW, allowing a dc current to pass through the device. At the pump frequency $\omega_p \approx 2\omega_0$, the stepped-impedance filter sections are half wavelength transmission lines, presenting the resonator with an impedance $R_{\rm eff} = R_e$. The full frequency dependence of $R_{\rm eff}$ is depicted in Fig. 1(b) (see Appendix A 3 for further discussion).

The resonator is realized using a segment of CPW featuring an interdigitated capacitor (IDC) [see Fig. 1(a)] terminated in a short circuit, and is designed to produce a resonance at the center of the band-stop (i.e., high-impedance) region $\omega_0/2\pi \approx 7.2$ GHz. The small CPW track width in the resonator ($w = 2\ \mu$m) reduces I_* and provides a sizable total kinetic inductance of $L_T = 3.84$ nH. The IDC adds additional capacitance to the resonator to decrease its characteristic impedance ($Z_0 \approx 118\ \Omega$) and subsequently enhance the pump current for a given pump power, which helps to minimize device heating. Furthermore, the IDC introduces dispersion to the resonator [27], detuning the higher-order modes away from harmonics of the fundamental (i.e., $3\omega_0$), preventing intermode coupling induced by the strong parametric pump [36]. The KIPA functions in the highly overcoupled regime, where the coupling rate to the port κ far exceeds the internal rate of loss γ.

To operate the KIPA, we feed the combined bias current $I_{\rm dc}$, signal, and pump into its port, as illustrated in Fig. 1(a). The tones mix inside the resonator and the resulting amplified and reflected signal is routed to a high-electron-mobility transistor (HEMT) amplifier at 4 K. This is followed by a third low-noise amplification stage at room temperature before being measured with a vector network analyzer (VNA) or undergoing homodyne detection (see Appendix B for details).

III. THE KIPA HAMILTONIAN

We have derived the Hamiltonian for the KIPA in the presence of the bias current $I_{\rm dc}$ and a pump tone $I_p \cos(\omega_p t + \varphi_p)$, expressed in a reference frame rotating at $\omega_p/2$:

$$H_{\rm KIPA}/\hbar = \underbrace{\Delta a^\dagger a + \frac{\xi}{2} a^{\dagger 2} + \frac{\xi^*}{2} a^2}_{H_{\rm DPA}/\hbar} + \underbrace{\frac{K}{2} a^{\dagger 2} a^2}_{H_{\rm Kerr}/\hbar}, \quad (3)$$

where Δ accounts for a frequency detuning of the KIPA from half the pump frequency $\omega_p/2$. $H_{\rm DPA}$ is the Hamiltonian for an ideal DPA [14]; it is quadratic in the field operators and is characterized by the 3WM strength ξ. $H_{\rm Kerr}$ represents the next higher-order term, which here is a self-Kerr interaction with strength K. See Appendix C for a detailed derivation of the Hamiltonian. Equation (3) is also the same approximate Hamiltonian found for 3WM-type JPAs, such as those that employ flux-pumped SQUIDs [15,17,37] or SNAILs [18–20]. An important quantity that largely determines the dynamic range and squeezing potential in these DPAs is the ratio $\kappa/|K|$, which quantifies the relative strength of $H_{\rm Kerr}$ to $H_{\rm DPA}$ [14,16,38] (since $|\xi| \to \kappa/2$ at large gain).

To quantify the Kerr interaction $|K| \propto \omega_0(\hbar\omega_0)/(I_*^2 L_T)$ for the KIPA (refer to Appendix C), we measure I_*. The dc bias current is swept in the absence of a pump tone, resulting in a shift of the device's resonance frequency [detected via its phase response; see Fig. 1(c)] that is related to the change in kinetic inductance described by Eq. (1). We observe a resonance frequency shift of approximately 100 MHz for a 0.9 mA bias, and extract $I_* = 5.10(9)$ mA from a fit of the current dependence. We estimate the Kerr constant for this device to be $|K|/2\pi \approx 0.13$ Hz, a completely negligible quantity relative to all other system parameters. We note that I_* is about three orders of magnitude greater than the critical current of a typical JPA, indicating a much weaker form of nonlinearity. This provides a ratio $\kappa/|K| > 10^8$ for the KIPA that is several orders of magnitude greater than that of a JPA [15–17].

We expect the 3WM strength in the KIPA, $|\xi| \propto \omega_0(I_{\rm dc} I_p/I_*^2)$ (see Appendix C), to be linear in the applied dc current. For the remainder of this paper, a bias current of $I_{\rm dc} = 0.834$ mA is used, close to the critical current of the film but leaving a sufficient margin for additional microwave currents to be applied through the pump and signal. The 3WM strength is somewhat independent of I_*,

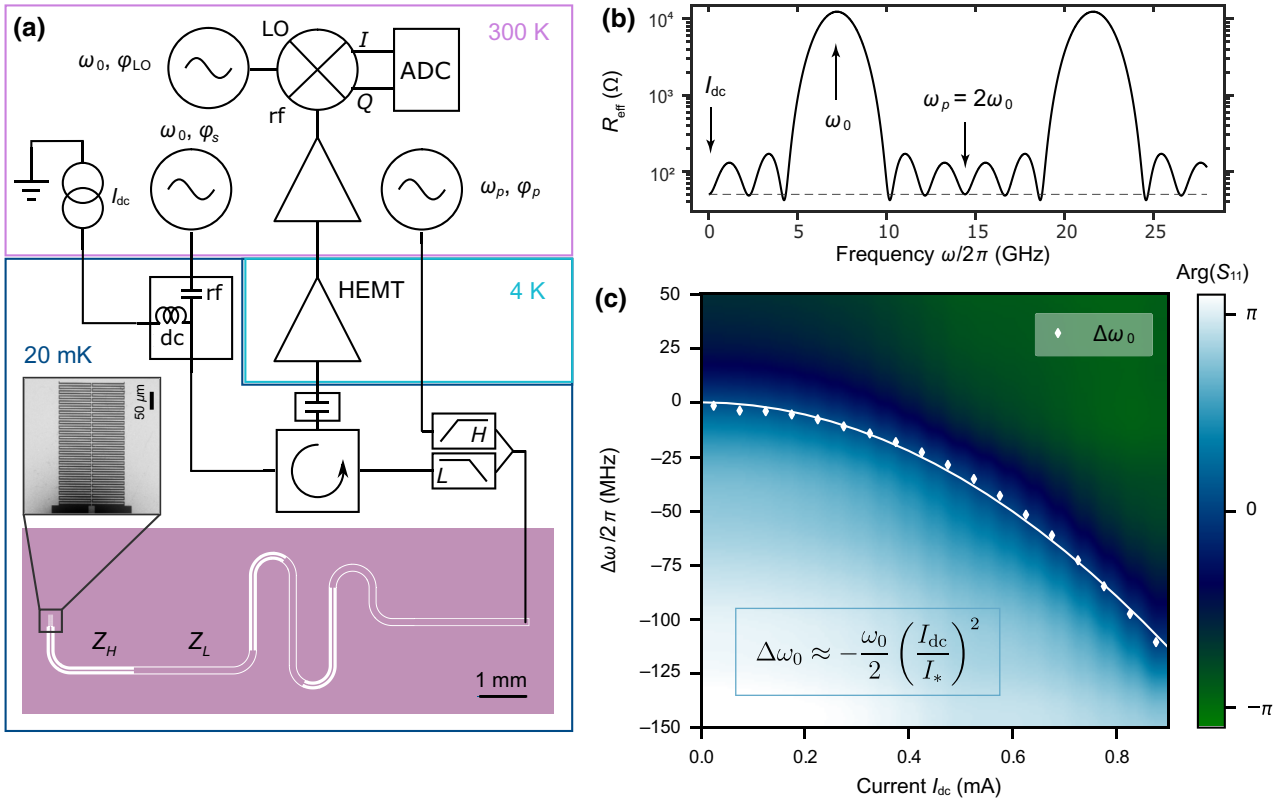

FIG. 1. Experimental setup and device geometry. (a) Experimental setup, showing the device pattern (bottom) and closeup optical microscope image of the interdigitated capacitor (IDC). The signal tone and bias current are combined at 20 mK using a bias tee. A diplexer mixes the pump and signal tones immediately before the sample. A circulator splits the forward microwave path from the reflected output of the device, which is measured at room temperature using homodyne detection (depicted) or with a vector network analyzer. (b) The effective impedance $R_{\rm eff}$ seen by the IDC resonator looking towards the port through the stepped-impedance filter. This impedance is high (approximately 12.8 kΩ) at the signal frequency (ω_0) and low (50 Ω) at the pump frequency ($\omega_p = 2\omega_0$). The filter passes dc and ω_p, and causes a strong reflection at ω_0. The dashed line indicates a 50-Ω impedance. (c) The phase response of the device versus bias current. The bias current shifts the resonant frequency over more than 100 MHz. Measured resonant frequencies at each current are presented (white diamonds), alongside a fit to the inset equation (solid white line).

since $I_{\rm dc}$ and I_p can always be raised to a sizable fraction of I_*, with the proviso that they are kept sufficiently small so that heating of the refrigerator and device does not occur.

Finally, it is important to mention that a large I_* alone is insufficient to explain why the KIPA is able to operate with such weak higher-order nonlinearities. For example, in a SQUID-based JPA it is known that increasing the critical current I_c of the SQUID loop similarly reduces $|K|$. However, it is also the case that increasing I_c simultaneously lowers the Josephson inductance $L_J \propto 1/I_c$. This presents challenges in practice, since L_J is quickly overwhelmed by the geometric inductance of the JPA. One can circumvent the issue by using arrays of SQUIDs [15]; however, this can be difficult to implement due to fabrication imperfections and challenges in achieving homogeneous flux control of a large SQUID array [16,38]. On the other hand, for a superconducting wire exhibiting kinetic inductance, one can control the scale of the current nonlinearity (I_*) independently of its inductance (L_T), by adjusting its geometric parameters (see the detailed discussion in Appendix C 4). Nonlinear currents I_* of the order of hundreds of microamperes to milliamperes can readily be attained while still maintaining practical kinetic inductances at the level of nanohenries.

IV. AMPLIFIER CHARACTERISTICS

Applying a pump tone at the frequency $\omega_p/2\pi = 14.381$ GHz and bias current $I_{\rm dc} = 0.834$ mA produces an amplification feature centered around $\omega_0/2\pi \approx 7.1905$ GHz [see Fig. 2(a)]. The KIPA generates an amplified signal tone ω_s at its output, along with an idler at ω_i such that energy is conserved in the 3WM process, $\omega_p = \omega_s + \omega_i$. The phase-insensitive gain, which occurs when the signal is not centered with respect to half of the pump frequency, that is, for $\omega_s = \omega_p/2 + \Delta\omega$ (with $|\Delta\omega|$ exceeding the resolution bandwidth of the measurement), increases with the pump power and is found to be in excess

of 40 dB before the KIPA crosses the threshold where spontaneous parametric oscillations occur (see Appendix E 3). To characterize the line-shape of the amplification feature, we assume that the KIPA operates as an ideal DPA (i.e., we assume $K = 0$) and derive the reflection parameter Γ using input-output theory [14]:

$$\Gamma(\omega) = \frac{\kappa(\kappa+\gamma)/2 + i\kappa(\Delta+\omega-\omega_p/2)}{\Delta^2 + \left[(\kappa+\gamma)/2 + i(\omega-\omega_p/2)\right]^2 - |\xi|^2} - 1 \tag{4}$$

(see Appendix E 1 for the derivation). We fit the gain data with the reflection model and observe excellent agreement with theory [see Fig. 2(a)]. We extract an average coupling quality factor of $Q_c = 135$, along with a constant gain-bandwidth product for the KIPA of 53(7) MHz.

When applying a signal tone at half the pump frequency $\omega_s = \omega_p/2$, the KIPA enters the degenerate mode of operation, producing phase-sensitive gain as the signal and idler tones interfere. Figure 2(b) depicts the gain of the KIPA as a function of the pump phase, where up to 26 dB of deamplification and close to 50 dB of amplification are measured. Compared to phase-insensitive amplification, additional gain is obtained in degenerate mode due to the constructive interference that occurs between the signal and idler.

After calibrating the phase of the pump to achieve maximum amplification (i.e., $\varphi_p \approx \pi/2$), we characterize the degenerate 1-dB compression point of the KIPA as a function of the gain [see Fig. 2(c)]. For approximately 20 dB of phase-sensitive gain, we find a 1-dB compression power of $-69.5(8)$ dBm at the device input, comparable to the performance of kinetic inductance traveling-wave amplifiers [24,27,39], despite the KIPA's resonant nature. The output power of the KIPA for this measurement was close to the input power 1-dB compression point of the cryogenic HEMT amplifier (approximately -46 dBm). It is thus possible that the true 1-dB compression point of the KIPA is even higher than we report here.

V. THE PHASOR TRANSFORMATION

The phase-dependent interference of the signal and idler fields in a DPA results in an affine transformation applied to the I-Q plane of the input field [5], which we refer to here as the phasor transformation. Figure 3(a) illustrates the distortion of the I-Q plane for coherent inputs that lie along a contour of constant amplitude, in addition to an equivalent transformation of a phase-space representation of a vacuum state input. The fields, which initially occupy a circular region on the I-Q plane, are stretched to form an ellipse, with the area being conserved in the process. Coherent states are useful for studying the phasor transformation since any noise field that couples into the cavity through the loss channel (γ) may be neglected (averaged away in a measurement), permitting a clear inspection of

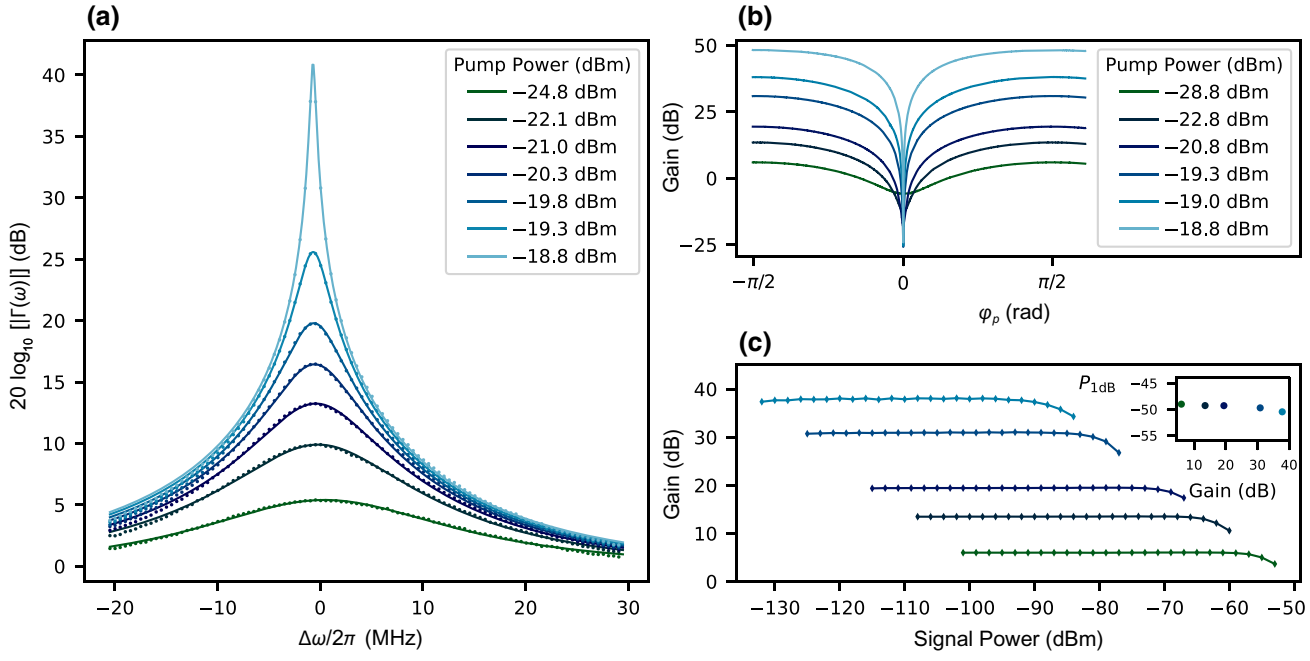

FIG. 2. Amplifier gain characteristics and compression with signal power. (a) Phase-insensitive gain as a function of the signal frequency $\omega = \Delta\omega + \omega_p/2$ for different pump powers (circles). The fitted theoretical frequency response is plotted (solid lines) with fitting parameters provided in Appendix E. (b) Phase-sensitive gain as a function of pump phase φ_p for various pump powers. The phase response has been aligned such that $\varphi_p = \pi/2$ corresponds to maximum gain. (c) Peak gain [found at $\varphi_p = \pi/2$ in (b)] as a function of signal power for the same pump powers shown in (b). Inset: output 1-dB compression power $P_{1\,\mathrm{dB}}$ as a function of gain.

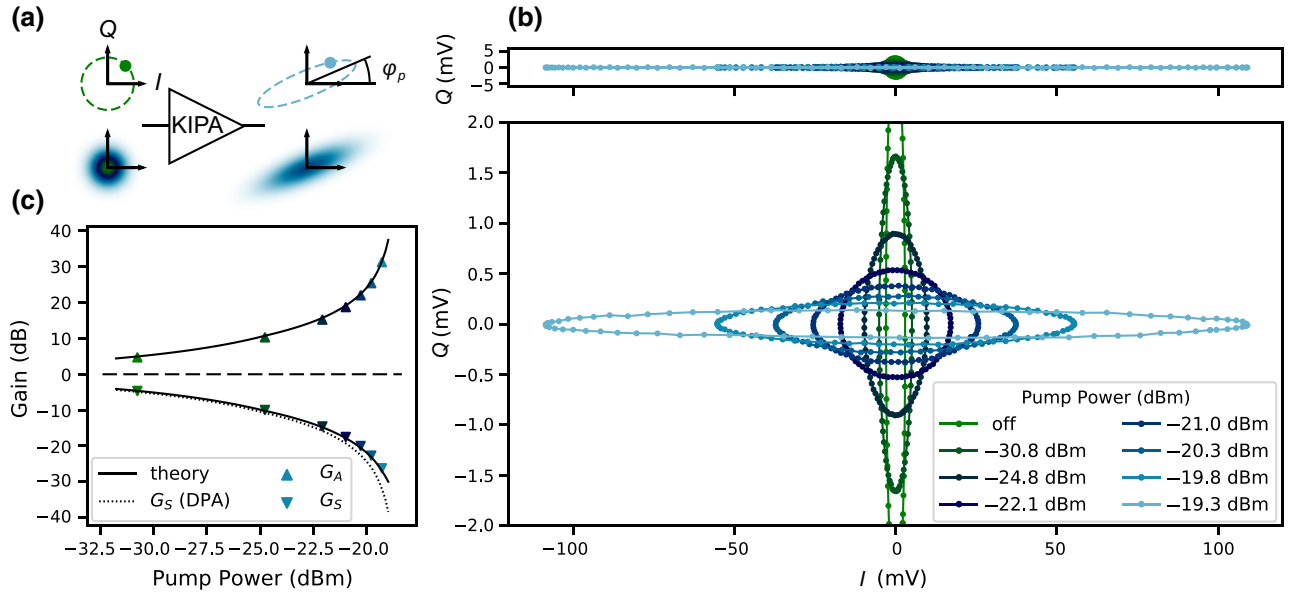

FIG. 3. The phasor transformation, measured with coherent inputs. (a) An illustration of the phasor transformation that similarly distorts the I-Q plane for coherent inputs (top) and the quasiprobability distribution of a quantum (vacuum) state (bottom). (b) KIPA response to coherent inputs of constant amplitude and varying phase, plotted on two different scales. Top: outputs are plotted with an equal aspect ratio, where the reflected input sweep with the KIPA off is observed as a circle (green) at the center of the plot. Turning the KIPA on stretches the circle to an ellipse, which resembles a blue line in this plot. Bottom: the same outputs plotted with a zoomed-in scale along Q so that the elliptical transformation may be observed. Solid lines are a guide for the eye. (c) The deamplification G_S and amplification G_A as a function of pump power. Points are extracted from the ellipses (b). The dotted line is the expected deamplification for an ideal DPA and the solid lines are the amplification and deamplification calculated with a model that includes small reflections along the measurement lines (see Appendix G 2).

any deviations from the expected transformation. Hamiltonian nonidealities manifest as an S-shaped distortion of the phase space at high gains, as has been experimentally observed [12,13] and modeled [14] in JPAs for gains typically exceeding approximately 10 dB.

We probe the phasor transformation by sweeping the phase of a coherent state incident on the KIPA and use homodyne detection to measure the transformed output. A coherent tone power of −112 dBm (corresponding to approximately 16 intracavity photons) was chosen to provide sufficient SNR without saturating the amplifier chain. Our results are shown in Fig. 3(b) for different pump powers. When the KIPA is off, sweeping the phase of the input coherent state traces out a circle on the I-Q plane. Activating the KIPA maps the circle to an ellipse at the detector with no noticeable S-type distortion, even for a degenerate gain of 30 dB. This exceeds the achievable phase-sensitive gain without distortion observed in JPAs by approximately two orders of magnitude. Further increases in gain (up to 50 dB) did not produce any obvious distortions, though at these higher gains the signal power had to be reduced to avoid saturating the cryogenic HEMT and room-temperature amplifiers, resulting in significant degradation in the SNR. The lack of S-type features at high gain supports the conclusion that the self-Kerr correction and other higher-order nonlinearities are negligible.

The deamplification level G_S is defined as the greatest reduction in amplitude of an input coherent state by the phasor transformation. We additionally define the amplification level G_A as being the corresponding increase in gain that occurs orthogonal to the axis of deamplification. G_S and G_A are measured after aligning the amplification and deamplification axes along I and Q, respectively, and averaging multiple measurements (refer to Appendix B 3 for details). Figure 3(c) presents the results, where up to 26 dB of deamplification is observed for 30 dB of amplification. Using the input-output theory for an ideal DPA, we derive the phasor transformation and predict G_S and G_A for the DPA parameters obtained from the fits in Fig. 2(a) (see Appendix G).

We observe some asymmetry $G_S \neq G_A$ in the data at high gains, as shown in Fig. 3(c), which we attribute to a small (approximately 2%) reflection occurring at the input to the KIPA (see Appendix G 2). This reflected signal adds to the deamplified coherent state and thus reduces the measured deamplification level. Such a reflection would occur for a 2-Ω impedance mismatch of the printed circuit board (PCB) to which the amplifier is connected, which is within its fabrication tolerances. Including a weak reflection along the signal path in our model accurately reproduces the slight asymmetry, as shown in Fig. 3(c). We note that the 26 dB of deamplification observed here represents an upper

bound to the amount of vacuum squeezing that can be expected in this device, which is sensitive to cavity losses, heating, and other effects. See Appendix H for a theoretical analysis of squeezing in the presence of cavity losses. Such high levels of noise squeezing, if realized, would be best exploited in on-chip applications, since any small amount of loss (e.g., in the PCB, diplexer, circulator, and cables) would mix in vacuum noise and lower the amount of squeezing. For example, an insertion loss in the range 1–2 dB on the output of the KIPA would already reduce 26 dB of vacuum noise squeezing to a level between 4.3 and 6.8 dB.

VI. NOISE PROPERTIES

We examine the noise performance of the KIPA by monitoring the output power of the setup on a spectrum analyzer. Figure 4(a) portrays a simplified noise model of the detection chain, with the KIPA amplifying an applied coherent state (i.e., a displaced vacuum). The following amplifiers and any loss along the output line are modeled by a single amplifier with a gain of G_T (refer to Appendix I 3). The parameters n_k and $n_{\rm sys}$ represent the number of noise photons added by each amplifier. A conversion factor z translates the dimensionless units of photons to an equivalent power in watts recorded on the spectrum analyzer. The measured output power can thus be converted to a number of photons at the input of the KIPA by dividing by the conversion factor zG_TG_k (i.e., $n_t = P_t/zG_TG_k$), where G_k represents the gain of the KIPA and is equivalent to the amplification level G_A when in degenerate mode. The factor zG_T is extracted from a detailed analysis of the output noise spectrum as a function of the KIPA's gain and temperature (see Appendix I 3). We note that this measurement makes the underlying assumptions that zG_T has negligible dependencies on the KIPA gain and temperature, which are not verified here. The following results should therefore be taken only as an initial estimate, with the noise performance to be accurately quantified in the future using a calibrated cryogenic noise source [27,40], which will permit measurements at fixed gain and temperature.

In Fig. 4(b) we plot the input-referred number of photons recorded in the presence of an applied coherent tone, with the KIPA in three different configurations: degenerate mode, nondegenerate mode, and off. Both the degenerate and nondegenerate measurements are taken at a pump power of $P_{\rm pump} = -19.3$ dBm, which provides gains of 31 dB and 24.5 dB, respectively. We observe an 18-dB enhancement in the SNR when operating in nondegenerate mode relative to using the HEMT as the first-stage amplifier (KIPA off) and an additional SNR enhancement of approximately 6 dB when operating in degenerate mode [see Fig. 4(b)], which is predicted [see Eqs. (I22) and (I27) in Appendix I 3] in the limit of large gain ($G_k \to \infty$) and for a near-quantum-limited noise performance. In

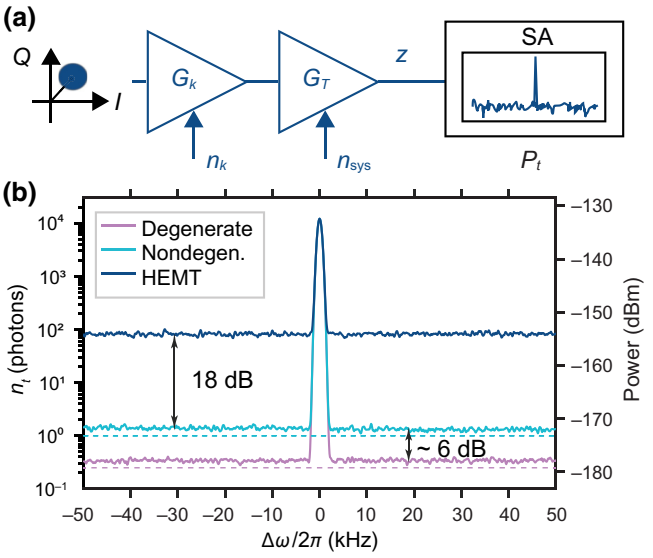

FIG. 4. Noise temperature characterization. (a) Schematic depicting a simplified detection chain that can be used to model the noise properties of the KIPA. The KIPA amplifies with a gain G_k, adding an amount of noise n_k. The following amplifiers and components are modeled as a single amplifier with a total gain of G_T and a noise contribution $n_{\rm sys}$. (b) Measured noise in the presence of a coherent tone, shown in units of power (dBm) and photons, referred to the input of the KIPA. The measurement is taken with a bandwidth resolution of 1 kHz. Traces were recorded with the KIPA in degenerate mode, nondegenerate mode, and off. In nondegenerate mode the signal-to-noise ratio is improved by 18 dB compared to a measurement using the cryogenic HEMT as the first amplifier. An additional 6-dB enhancement is observed when the KIPA is in degenerate mode. The quantum noise limit is indicated by dashed lines for each mode of operation.

the degenerate measurement of Fig. 4(b), the noise floor indicates an input-referred noise of approximately 0.35 photons, close to the quantum limit of 0.25 photons. It should be noted that this measurement contains contributions to the noise from all sources, including from the following amplifiers. Finally, it is useful to estimate the noise referred to the rf input of the bias tee [see Fig. 1(a)], where a device under test would ultimately be connected. The typical manufacturer-specified insertion loss of the components and cables between the rf input and the KIPA port (see Appendix B for details) at room temperature is 3.5 dB, which provides a bias tee input-referred noise of 0.78 photons.

VII. DISCUSSION

We have presented a simple and versatile microwave parametric amplifier called a KIPA, fabricated from a thin film of $Nb_xTi_{1-x}N$. For the parameter space tested, we report above 40 dB of phase-insensitive gain and up to 50 dB of phase-sensitive gain. Our device features

an exceptionally high input 1-dB compression point of −69.5 dBm for 20 dB of gain. Using input-output theory, we have been able to model our device using the Hamiltonian of an ideal DPA, with excellent agreement between theory and experiment. The close DPA approximation indicates that the KIPA might also serve as an effective microwave squeezer, which we study through mapping its phasor transformation out to $G_A = 30$ dB. Our first attempt to measure the noise properties of the KIPA indicates that it operates close to the quantum limit; however, further measurements using a calibrated noise source should be performed to verify its performance.

Both the power-handling capability of the KIPA acting as an amplifier and its potential to serve as a squeezer benefit from its reduced self-Kerr strength $|K|$ relative to the resonator bandwidth κ (i.e., the large ratio $\kappa/|K|$). The stepped-impedance filter design allows us to achieve a large κ, despite the resonator impedance being relatively high ($Z_0 \approx 118\ \Omega$) due to the sizable kinetic inductance, and should be amenable to designs with even greater κ. The kinetic inductance provides a scaling of the nonlinear current and inductance that allows large values of I_* while maintaining practical inductances L_T, which is crucial here to minimize $|K|$.

Future experiments will focus on exploring the noise-squeezing properties of the KIPA by using a second KIPA as a following amplifier [10,12]. The large levels of deamplification without distortion observed here set an upper bound to its noise- squeezing capabilities as any loss present will act to mix in the vacuum state and reduce squeezing, with an ultimate limit (as would be expected directly at the KIPA output) set by the ratio $Q_c/Q_i = \gamma/\kappa$ (see Appendix H). Amplification also benefits from a small Q_c/Q_i, as it permits a noise performance closer to the quantum limit. We note that planar $Nb_xTi_{1-x}N$ resonators can reach exceptionally large internal quality factors ($Q_i > 10^6$ [33,41]), making this an attractive system for performing low-noise amplification and noise squeezing.

Squeezed vacuum states are a valuable resource in quantum computing [42]. Measurement-based computation using highly entangled cluster states encoded in the modes of an electromagnetic field is one possible pathway to achieving large-scale quantum computation [43]. It has been shown that squeezing levels in excess of 17 dB would surpass the fault-tolerant threshold for quantum computation in such a scheme [44]. Circuit-based microwave squeezers are a particularly attractive platform in this context, as they combine circuit manufacturability with another key requirement in cluster-state computing; the ability to engineer non-Gaussian states of light [45–47]. To generate this level of direct squeezing with the KIPA, in addition to minimizing Q_c/Q_i one must circumvent the insertion loss of the components connected along the signal output path. This could be achieved by spatially separating the signal input and output from the pump and dc bias by moving to a two-port architecture with high coupling asymmetry, or utilizing on-chip circulators [48–51] to avoid transferring the squeezed states off-chip all together.

The high dynamic range and large levels of gain attained with the KIPA could make it useful for measuring small signals (e.g., in the readout of superconducting qubits) without the need for a 4-K HEMT amplifier, though its current bandwidth and tunability make it unsuitable for multiplexed qubit measurements. The large 1-dB compression point power could also find it application in reflectometry measurements for spin qubit readout [52], where the signal-to-noise ratio can be enhanced for signal powers up to −80 dBm in devices [53], powers that exceed the available dynamic range in JPAs. Finally, high-kinetic-inductance $Nb_xTi_{1-x}N$ resonators can display excellent magnetic field compatibility, with $Q_i > 10^5$ at fields up to 6 T reported [31]; we therefore envisage utilizing this amplifier in applications such as electron spin resonance spectroscopy, where the KIPA can serve as both the microwave cavity and first-stage amplifier to push the boundary of spin detection sensitivity [54,55].

ACKNOWLEDGMENTS

J.J.P. is supported by an Australian Research Council Discovery Early Career Research Award (DE190101397). J.J.P. and A.M. acknowledge support from the Australian Research Council Discovery Program (DP210103769). A.L.G. is supported by the Australian Research Council, through the Centre of Excellence for Engineered Quantum Systems (CE170100009) and Discovery Early Career Research Award (DE190100380). A.M. is supported by the Australian Department of Industry, Innovation and Science (Grant No. AUSMURI000002). W.V. acknowledges financial support from the Sydney Quantum Academy, Sydney, NSW, Australia. This research has been supported by an Australian Government Research Training Program (RTP) Scholarship. The authors acknowledge support from the NSW Node of the Australian National Fabrication Facility. We thank Robin Cantor and STAR Cryoelectronics for sputtering the $Nb_xTi_{1-x}N$ film. The authors thank Nicolas Menicucci and Patrice Bertet for helpful discussions.

APPENDIX

APPENDIX A: DEVICE DESIGN

1. Fabrication

The KIPA is fabricated on a 350-μm-thick high-resistivity silicon wafer. The wafer is cleaned with a piranha solution (a mixture of sulfuric acid, water, and hydrogen peroxide) followed by a hydrofluoric acid etch of the natural silicon dioxide before having a 9.5-nm-thick film of $Nb_xTi_{1-x}N$ sputtered on the surface (STAR

Cryoelectronics). To define the pattern we perform a standard electron beam lithography process using AR-P 6200 (9%) as a positive resist. Reactive ion etching (RIE) with CF_4 and Ar is used to etch the $Nb_xTi_{1-x}N$ in the exposed regions of the chip. After the RIE step any residual resist mask is removed using solvents before the device is bonded to a PCB and measured.

2. Material choice

In principle, most low-loss and high-kinetic-inductance materials would be suitable for constructing a KIPA. The resonator should have a kinetic inductance that forms a sizable fraction of the total inductance, since the geometric inductance does not facilitate mixing and thus increases the pump power requirements for amplification. Examples of potential superconductors in which this might be achieved include niobium nitride (NbN), titanium nitride (TiN), and molybdenum-rhenium (MoRe). See the review by Mazin [56] on materials for kinetic inductance detectors for a more comprehensive list.

In addition, the current nonlinearity strength I_* must be large enough to provide sufficient dynamic range, but small enough to avoid heating due to excessive pump powers. I_* is related to the critical current I_c and is determined by the material parameters (such as the superconducting gap energy and normal state resistivity) as well as geometry (e.g., the resonator wire cross-sectional area) [29]; see Appendix C 4 for further details. To achieve substantial gains, the pump current must reach a sizable fraction of I_*, typically $I_p \approx 0.1 I_*$, which implies pump powers of $P_p = I_p^2 Z_0/2 \approx I_*^2 Z_0/200$ (where Z_0 is the resonator impedance) should be applied. For a resonator impedance of the order of 50 Ω and pump powers below the base cooling power of a typical dilution refrigerator (approximately 10 μW), practically we are limited to $I_* \lesssim 6$ mA, with critical currents typically a few factors lower than this, $I_c \lesssim 2$ mA. For our 9.5-nm-thick $Nb_xTi_{1-x}N$ film, we find a critical current of order 1 mA for a wire width of 2 μm. Using superconductors with larger gap energies (and thus higher critical current densities and critical temperatures) than $Nb_xTi_{1-x}N$ may present challenges with heating and would likely require smaller resonator wire geometries. However, superconductors with critical temperatures below niobium titanium nitride that exhibit both a high normal state resistivity (i.e., high kinetic inductance) and low loss could in principle be utilized to make a KIPA.

3. Stepped-impedance filter

The stepped-impedance filter is comprised of alternating sections of a high-impedance CPW transmission line (with impedance Z_H and length l_H) and low-impedance CPW transmission line (with impedance Z_L and length l_L). One "cell" is made from a single Z_H section followed by a Z_L section. The filter contains $N = 3$ cells in total and is galvanically connected to the shorted quarter-wavelength IDC resonator (see Appendix A 6). On the source side, the stepped-impedance filter sees a $R_e = 50$ Ω environment. See Fig. 5(a) for a transmission-line model of the device.

The lengths l_H and l_L are chosen to equal a quarter-wavelength at the resonator fundamental frequency ω_0. For $\omega \approx \omega_0$ these sections therefore act like quarter-wavelength transformers, which transform the environmental impedance R_e to

$$R_{\text{eff}} = \left(\frac{Z_H}{Z_L}\right)^{2N} R_e, \tag{A1}$$

as seen by the quarter-wavelength IDC resonator.

On the other hand, at the pump frequency $\omega_p \approx 2\omega_0$, the high- and low-impedance segments are half wavelength transmission lines, providing

$$R_{\text{eff}} = R_e. \tag{A2}$$

More precisely, we may solve for the frequency dependence of R_{eff} by calculating the ABCD matrix of the stepped-impedance filter and external environment, from which we can determine the admittance matrix and input admittance Y_{in} observed by the IDC resonator [17,57]. This produces in an effective impedance of

$$R_{\text{eff}}(\omega) = \frac{1}{\text{Re}\{Y_{\text{in}}(\omega)\}}. \tag{A3}$$

The resulting $R_{\text{eff}}(\omega)$ is plotted in Fig. 1(b). Close to the resonant frequency ω_0, the IDC quarter-wavelength shorted resonator can be modeled as a lumped-element *RLC* parallel circuit with the following parameters [58]:

$$R_i = \frac{Z_0}{\alpha l_0}, \tag{A4}$$

$$L = \frac{1}{\omega_0^2 C}, \tag{A5}$$

$$C = \frac{\pi}{4\omega_0 Z_0}, \tag{A6}$$

where α is the complex component of the transmission-line propagation constant and characterizes the resonator loss. See Fig. 5(b) for the equivalent circuit model. We can thus define the internal and external quality factor of the resonator as

$$Q_i = \frac{R_i}{\omega_0 L}, \tag{A7}$$

$$Q_c = \frac{R_{\text{eff}}}{\omega_0 L}. \tag{A8}$$

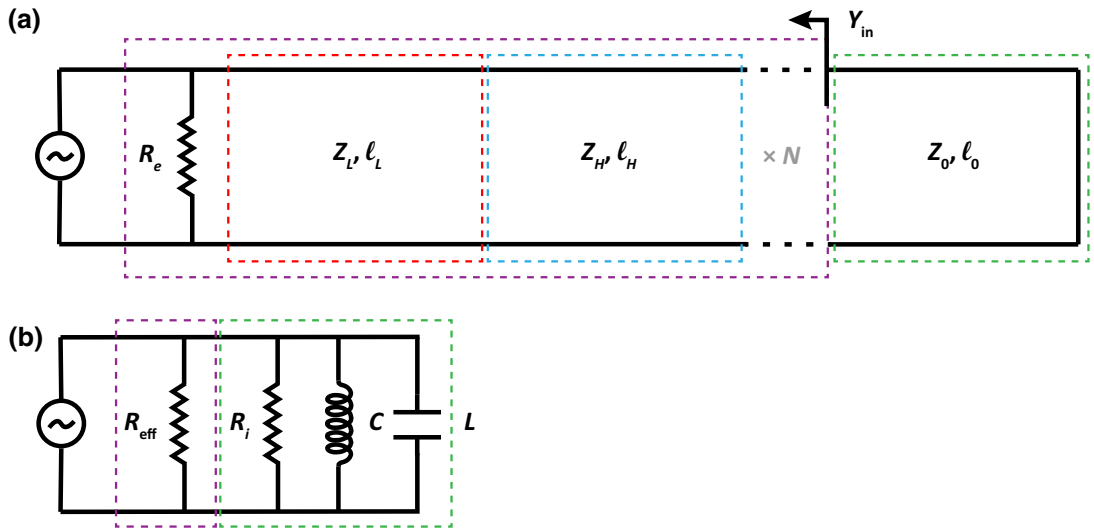

FIG. 5. (a) Transmission-line model of the stepped-impedance filter and quarter-wavelength resonator. The red dashed box indicates one instance of the low-impedance transmission-line segment (impedance Z_L), the blue dashed box indicates one instance of the high-impedance transmission-line segment (impedance Z_H), and the purple dashed box identifies the effective admittance seen by the quarter-wavelength resonator. The green dashed box represents the shorted quarter-wavelength interdigitated capacitor resonator (impedance Z_0). (b) An LC model of the quarter-wavelength resonator close to its resonant frequency ω_0 and the effective impedance presented by the stepped-impedance filter and 50-Ω external environment.

Taking the effective impedance seen by the resonator at $\omega = \omega_0$ [Eq. (A1)], we find the external quality factor:

$$Q_c = \left(\frac{Z_H}{Z_L}\right)^{2N} \frac{\pi R_e}{4Z_0}. \tag{A9}$$

Inserting the impedances used in our device ($Z_H = 126\ \Omega$, $Z_L = 50\ \Omega$, $R_e = 50\ \Omega$, and $Z_0 = 118\ \Omega$) into Eq. (A9), we expect $Q_c \approx 85$. In the experiment we measure $Q_c \approx 135$, in close agreement with theory. We note that the external quality factor has a strong dependence on the impedance ratio Z_H/Z_L and any small error in this quantity will have a large effect on Q_c.

4. Estimating the kinetic inductance L_0

To target specific impedances we first need to know the "per-square" kinetic inductance of the niobium titanium nitride film $L_\square$. We estimate $L_\square$ by measuring a test quarter-wavelength resonator and determining its resonant frequency. We perform a simulation of the same device (using the software Sonnet) and adjust $L_\square$ until we obtain the measured resonance frequency ω_0, which occurs for our 9.5-nm-thick film when $L_\square = 32$ pH. Dividing the per-square kinetic inductance by the resonator wire width provides the per-unit-length kinetic inductance $L_0 = L_\square/w$.

5. Bandwidth

It should in principle be possible to design KIPAs with larger bandwidths by reducing the impedance ratio Z_H/Z_L or the number of cells N (Appendix A 3). However, in order to achieve the same high levels of gain observed in the present device (i.e., > 40 dB) the 3WM strength $|\xi|$ [Eq. (C34d)] must be increased proportionally [see Eq. (E1) for a relation between gain and $|\xi|$]. At present, we believe we are approaching the limit of the pump power that can be applied (and therefore $|\xi|$) before device and refrigerator heating become an issue. This could be partially resolved by lowering the resonator impedance, which will produce a larger pump current for a given power. Apart from this, one could lower I_* by using thinner $Nb_xTi_{1-x}N$ films or narrower resonator wires, both of which should be possible. Lowering I_* would unavoidably increase the Kerr strength $|K|$ [Eq. (C34c)], but its small value in the current device (see Appendix C 3 for an estimation of $|K|$) indicates that this is a worthwhile tradeoff. We believe an order-of-magnitude enhancement in the bandwidth to be achievable with careful device optimization.

6. Quarter-wavelength IDC resonator

The short-circuit-terminated quarter-wavelength resonator is implemented with a CPW that features a dense interdigitated capacitor to ground (see Fig. 6). The IDC serves to lower the impedance of the resonator, bringing it closer to the 50-Ω port impedance and reducing reflections at the pump frequency. In addition, the smaller impedance produces a larger pump current for a given pump power. Both of these effects help to reduce device heating by lowering the pump power requirements.

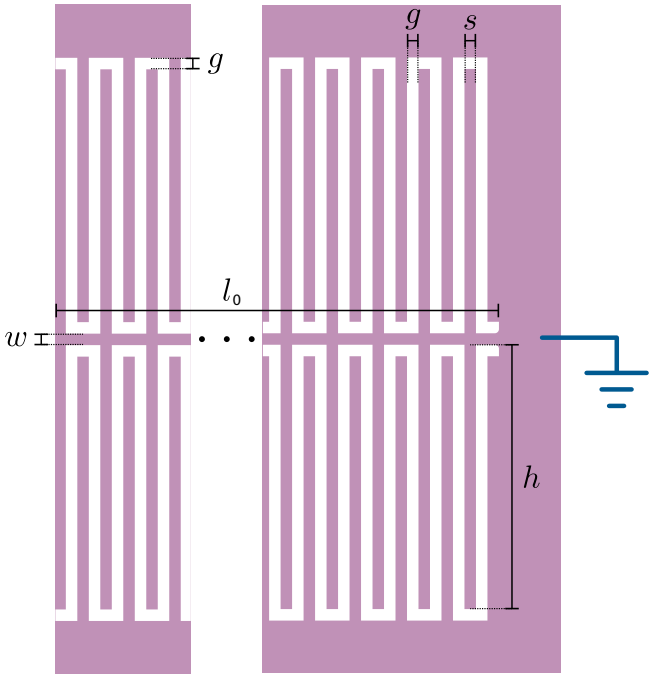

FIG. 6. Sketch of the IDC quarter wavelength resonator employed in the KIPA. The stepped-impedance filter is galvanically connected to the left side of this schematic. This element has the smallest track width and hence the lowest I_*, presenting the largest nonlinearity of any section in the device.

The resonator has a length of $l_0 = 240$ μm and the inner track is $w = 2$ μm wide. The capacitor fingers are $s = 2$ μm wide and $h = 46$ μm long, with a $g = 2$ μm gap to the ground plane. This provides a resonator impedance (estimated from Sonnet simulations) of approximately $Z_0 \approx 118$ Ω.

APPENDIX B: EXPERIMENTAL SETUP

All measurements are performed with the device situated at the mixing chamber plate ($T \sim 20$ mK) of a dilution refrigerator. A schematic of the setup is shown in Fig. 7, with components described in detail in the subsections that follow.

1. Wiring

Pump line. A microwave source (E8267D, Keysight Technologies) supplies the pump tone for all experiments via a high-pass filter (HFCN-9700+, Mini-Circuits) used to reduce microwave source subharmonics. A 10-dB cryogenic attenuator is used at the 4-K temperature stage, followed by two 3-dB attenuators at the 900-mK and 100-mK stages, respectively. The pump line connects to the KIPA via a diplexer (DPX-1114, Marki Microwave) at the 20-mK stage (shown in Fig. 7), which provides rejection exceeding 40 dB at the signal frequency $\omega_0/2\pi = 7.2$ GHz.

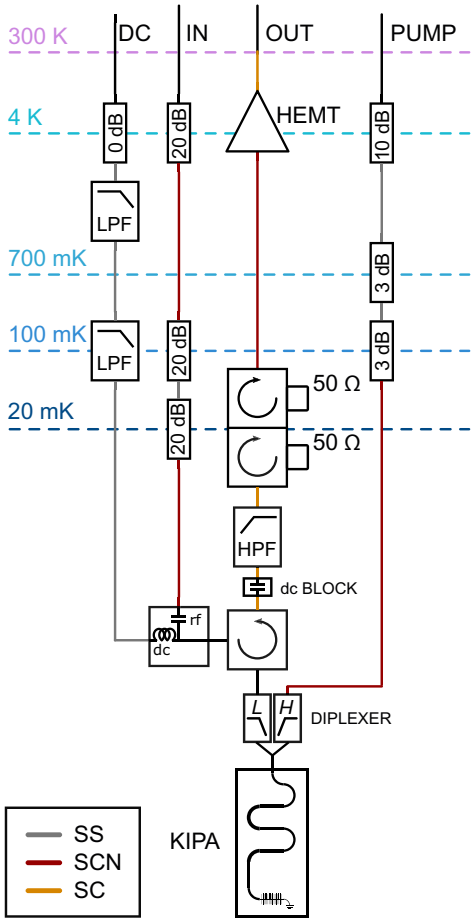

FIG. 7. Schematic depicting the cryogenic experimental setup. SS, stainless steel coaxial cable; SCN, silver-plated cupronickel coaxial cable; SC, silver-plated copper coaxial cable.

Signal line. Three 20-dB attenuators are used to minimize the transmission of thermal noise to the device, and are situated at the 4-K, 900-mK, and 20-mK stages, respectively. The signal line then connects to the rf port of the bias tee (PE1615, Pasternack Enterprises), as shown in Fig. 7.

Direct current line. The dc line connects to the bias tee via a 1-dB attenuator at 4 K and two low-pass filters at 4 K and 100 mK (VLF-7200+ and VLF-105+, Mini-Circuits Technologies), blocking room-temperature noise at pump and signal frequencies. The dc line breaks out to a copper wire that is thermalized to a bobbin fixed to the 20-mK plate before connecting to the dc port of a bias tee (shown in Fig. 7).

Detection path. A cryogenic circulator (Quinstar Technology, CTH0508KCS) routes the reflected output of the KIPA through the detection chain. The circulator has a typical isolation of 18 dB at the amplifier frequency ($\omega_0/2\pi = 7.2$ GHz) and an insertion loss of 0.5 dB. A high-rejection bandpass filter (Micro-Tronics Inc, BPC50403-01) immediately follows and attenuates any power at the pump

frequency that may leak through the diplexer. A double isolator (Quinstar Technology, CTH0508KCS $\times 2$) at 20 mK connects the output of the bandpass filter to a cryogenic HEMT low-noise amplifier (Low Noise Factory, LNF-LNC0.3_14A) situated at 4 K.

2. VNA measurements

Port 1 of a vector network analyzer (Rohde & Schwarz, ZVB-20) is connected to the signal line via an attenuator, used to reduce the minimum signal power of the network analyzer. We use a low-noise amplifier (Mini-Circuits, ZX60-06183LN+) at the output of the detection chain, which connects to port 2 of the VNA.

The data presented in Fig. 1(c) were collected with the pump source disabled. We apply a dc voltage (Yokogawa Electric, GS2000) to the dc line, in series with an approximately 10-kΩ resistor at room temperature. We observe a 2π phase shift in the frequency response measured with the VNA, as expected for a $\lambda/4$ resonator measured in reflection in the overcoupled regime (see Appendix E 1). A linear fit to the first 100 MHz of the phase response is used to estimate the line delay of our setup and is subtracted from the complete phase response. The phase is then increased by π to correct for the expected phase offset that is removed by the fit to the line delay. To model the resonance frequency shift, we fit a quadratic polynomial to the resonance frequency as a function of the square of the current.

The 14.318-GHz pump is then enabled with a 0.834-mA dc bias current for the measurement of the phase-insensitive gain in Fig. 2(a). We use the VNA to probe the magnitude response about half the pump frequency. To estimate the baseline of the magnitude response, we disable the pump but leave the bias current active, which yields an approximately flat magnitude response (see Appendix J). We subtract the magnitude response of the baseline measurement from the magnitude response of the gain curve to obtain the data presented in Fig. 2(a). For an detailed explanation of the fitting procedure, refer to Appendix E.

To study the phase-sensitive gain, we operate the ZVB-20 as a spectrum analyzer, using it to measure the incident power on port 2. The signal line is connected to another E8267D microwave source (Keysight Technologies) via an attenuator and is configured for linear phase modulation at half the pump frequency (7.1905 GHz) and approximately -112 dBm of signal power at the sample. The pump and signal sources are phase locked using a 1-GHz reference clock. With the VNA configured for a zero-span measurement and triggered off the edge of each phase ramp, we obtain the data presented in Fig. 2(b). Again we disable the pump, measure the baseline, and subtract the mean reflected baseline power from each measurement to obtain the phase-sensitive gain. Due to slow phase drifts between the VNA local oscillator and the signal tone, we repeat each measurement 40 times, and use the maximum of the cross-correlation between pairs of traces to align the data before averaging. We repeat this measurement for a range of signal powers and pump powers, and use the maximum of the gain curve to define the degenerate gain, as presented in Fig. 2(c). The compression power is determined by the signal power where the presaturation gain drops by 1 dB. We define the presaturation gain by the average of the degenerate gains measured for the ten smallest signal powers.

3. Coherent state measurement

For the remainder of the measurements, the output of the detection chain is connected to a homodyne detection setup consisting of an I-Q mixer (Marki Microwave, IQ4509), with the local oscillator supplied by another independent ultralow-phase-noise microwave source (Keysight Technologies, E8267D) which is phase-locked with a 1-GHz reference clock to the pump and signal sources. The local oscillator frequency is set to 7.1905 GHz. The I and Q outputs of the mixer connect to 1.9-MHz low-pass filters (Mini-Circuits, SLP-1.9+) followed by two $5\times$ preamplifiers (Stanford Research Systems, SIM914) connected in series. I and Q are then digitized using a data acquisition card (Keysight Technologies, M3300A) configured with a sample rate of 6.25 MHz.

The ellipse measurements [depicted in Fig. 3(b)] were performed with the pump and local oscillator phases fixed, while the signal phase is stepped. Each (I, Q) pair is measured by averaging 10^6 samples collected at each phase. The entire phase sweep is performed in less than 60 s to minimize errors due to slow phase drift between the signal and pump. Before each measurement, we calibrate the phase of the local oscillator by rotating the I-Q plane in software to measure the angle that produces the least variance on Q. We refine phase calibration by repeating the procedure three times in order to ensure measurement consistency despite small channel imbalances between I and Q. We measure 16 repetitions of the phase sweep and software-rotate each data set to further minimize the variance on Q due to slow phase drifts in the setup. The repetitions are aligned by maximizing the pairwise cross-correlation of I (Q) as a function of the signal phase, and then averaged to produce the data presented in Fig. 3(b).

We interleave a measurement with the pump off to measure the circular response of the reflected signal in the I-Q plane. We measure G_S (G_A) by taking the ratio of the peak-to-peak amplitudes of the pump-off response and pump-on response for Q (I) after averaging. These results are plotted in Fig. 3(c). Phase calibration is performed with the pump on, and the calibration phase is kept after the pump is disabled.

4. Noise measurements

To collect the data presented in Fig. 4, we replace the room-temperature amplifier with a low-noise HEMT amplifier (Low Noise Factory, LNF-LNR1_15A) for improved noise performance.

APPENDIX C: HAMILTONIAN OF A KINETIC INDUCTANCE PARAMETRIC AMPLIFIER

1. Zero bias

A kinetic inductance can be described as a nonlinear inductance

$$L_k(I) = L_0\left(1 + \frac{I^2}{I_*^2}\right). \tag{C1}$$

We consider a "telegrapher's model" for a kinetic inductance resonator, as illustrated in Fig. 8(a), and wish to write down the Lagrangian for this system. The circuit has a capacitance C and kinetic inductance $L_k(I)$ per unit length. We assume that the kinetic inductance is far greater than the geometric inductance (L_g) along the transmission line (i.e., $L_0 \gg L_g$). Because the inductance depends on current, and current is related to charge in a straightforward manner, we find it convenient in this situation to formulate the Lagrangian with charge as the coordinate. We therefore use the "loop charge" approach described in Ref. [59]. The loop charges are related to the current across the inductors and charge on the capacitors through

$$I_n = \dot{Q}_n, \tag{C2}$$

$$q_n = Q_n - Q_{n-1}, \tag{C3}$$

respectively. Note that in this particular geometry, the loop charge equals the cumulative charge $Q_n = \sum_{k=0}^{n-1} q_k$.

Applying Kirchhoff's voltage law around a single loop in the telegrapher's circuit model [see Fig. 8(b)] yields

$$\begin{aligned} V(x+\Delta x,t) &= V(x,t) + L_k(I_n)\Delta x \dot{I}_n, \\ \frac{V(x+\Delta x,t) - V(x,t)}{\Delta x} &= L_k(I_n)\dot{I}_n, \\ \to \partial_x V(x,t) &= L_k(I)\partial_t I, \end{aligned} \tag{C4}$$

where in the third line we take a continuum limit $\Delta x \to 0$. This is the well-known telegrapher's equation, with a nonlinear inductance as provided in Eq. (C1), and describes the relevant equation of motion for our circuit. The telegrapher's equation can equivalently be expressed as

$$\frac{1}{C}\partial_x^2 Q(x,t) = L_k(\partial_t Q)\partial_t^2 Q, \tag{C5}$$

with $I = \partial_t Q$. The Lagrangian for the system that reproduces the telegrapher's equation with its Euler-Lagrange equation is found to be

$$\begin{aligned} \mathcal{L}_{\mathrm{KIPA}} &= \frac{1}{2}\sum_{n=0}^{N-1}\left[L_0\Delta x\left(1 + \frac{1}{6}\frac{\dot{Q}_n^2}{I_*^2}\right)\dot{Q}_n^2 \right. \\ &\quad \left. - \frac{1}{C\Delta x}(Q_{n+1} - Q_n)^2\right], \\ &\to \frac{1}{2}\int_0^l dx\left[L_0\left(1 + \frac{1}{6}\frac{(\partial_t Q)^2}{I_*^2}\right)(\partial_t Q)^2 \right. \\ &\quad \left. - \frac{1}{C}(\partial_x Q)^2\right], \\ &= \frac{1}{2}\int_0^l dx\left[L_0(\partial_t Q)^2 - \frac{1}{C}(\partial_x Q)^2\right] \\ &\quad + \frac{L_0}{12I_*^2}\int_0^l dx(\partial_t Q)^4, \end{aligned} \tag{C6}$$

where in the third line we once again take a continuum limit $\Delta x \to 0$. We note that this form of the Lagrangian differs from the work of Ref. [60], but correctly reproduces the classical telegrapher's equations for a kinetic inductance transmission line [Eq. (C5)] assumed in recent work [27,30].

The canonical momentum corresponding to Q is

$$\Phi = \frac{\partial \mathcal{L}_{\mathrm{KIPA}}}{\partial \dot{Q}} = L_0\partial_t Q + \frac{L_0}{3I_*^2}(\partial_t Q)^3, \tag{C7}$$

and the Hamiltonian is given by

$$\begin{aligned} H &= \int_0^l dx \Phi \partial_t Q - \mathcal{L} \\ &= \frac{1}{2}\int_0^l dx\left[L_0(\partial_t Q)^2 + \frac{1}{C}(\partial_x Q)^2\right] \\ &\quad + \frac{3L_0}{12I_*^2}\int_0^l dx(\partial_t Q)^4. \end{aligned} \tag{C8}$$

To express this in terms of Φ and Q we use the approximation

$$\begin{aligned} \partial_t Q &= \frac{1}{L_0}\Phi - \frac{1}{3I_*^2}(\partial_t Q)^3 \\ &= \frac{1}{L_0}\Phi - \frac{1}{3I_*^2 L_0^3}\Phi^3 + \mathcal{O}\left(\frac{1}{I_*^4}\right) \end{aligned} \tag{C9}$$

and

$$(\partial_t Q)^2 \simeq \frac{1}{L_0^2}\Phi^2 - \frac{2}{3I_*^2 L_0^4}\Phi^4, \tag{C10a}$$

$$(\partial_t Q)^4 \simeq \frac{1}{L_0^4}\Phi^4. \tag{C10b}$$

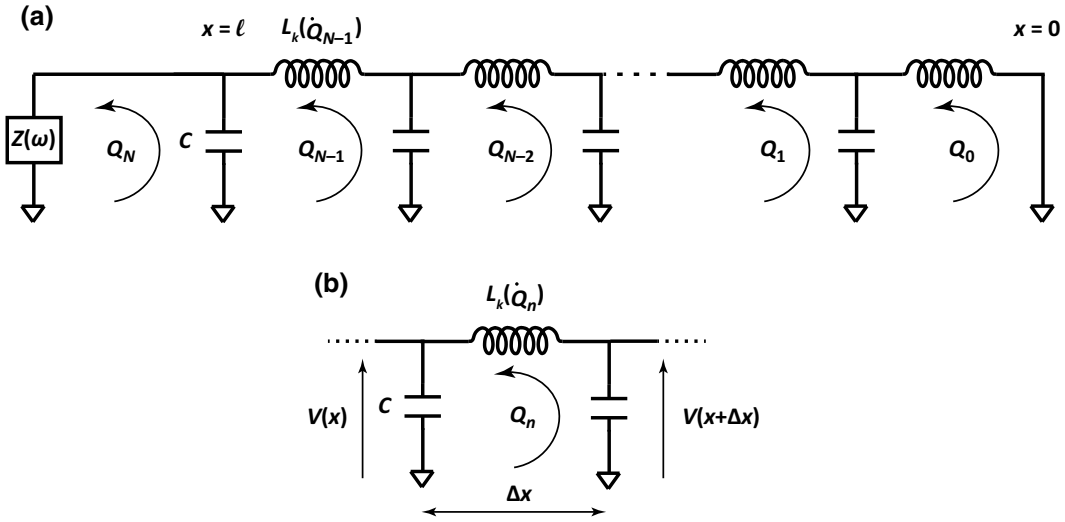

FIG. 8. (a) Telegrapher's model of a kinetic inductance resonator. (b) A single loop of the telegrapher's model.

Thus, to first order in $1/I_*^2$ we find

$$H_{\mathrm{KIPA}} = H_0 + H_1, \tag{C11a}$$

$$H_0 = \frac{1}{2}\int_0^l dx \left[\frac{1}{L_0}\Phi^2 + \frac{1}{C}(\partial_x Q)^2\right], \tag{C11b}$$

$$H_1 = -\frac{1}{12 I_*^2 L_0^3}\int_0^l dx \Phi^4. \tag{C11c}$$

a. Mode expansion for the quarter-wavelength resonator

We start by finding the mode functions of a linear ($I_* \to \infty$) $\lambda/4$ resonator. In this case, the Euler-Lagrange equation corresponding to $\mathcal{L}_{\mathrm{KIPA}}$ is the telegrapher's equation,

$$v_0^2 \partial_x^2 Q = \partial_t^2 Q, \tag{C12}$$

with $v_0 = 1/\sqrt{L_0 C}$ the linear phase velocity.

The $\lambda/4$ resonator is shorted at $x = 0$ corresponding to a boundary condition of zero voltage, or $(Q_1 - Q_0)/C\Delta x \to \partial_x Q(x=0)/C = 0$ in the continuum limit. At $x = l$ we leave the boundary condition general by taking an impedance $Z(\omega)$ to ground and imposing Ohm's law $V(x=l) = -Z(\omega) I(x=l)$ (for an I convention defined in Fig. 8) at the boundary, with $V(x=l) = \partial_x Q(x=l)/C$ and $I(x=l) = \partial_t Q(x=l)$. In summary,

$$\partial_x Q(x=0) = 0 \quad \text{(short circuit)}, \tag{C13a}$$

$$\partial_t Q(x=l) = -\frac{1}{Z(\omega) C}\partial_x Q(x=l) \quad [\mathrm{Z}(\omega) \quad \text{to ground}]. \tag{C13b}$$

An open (short) boundary condition at $x = l$ is recovered in the limit $Z(\omega) \to i\infty$ [$Z(\omega) \to i0$].

We use an ansatz,

$$Q(x,t) = i\sum_m A_m \cos(k_m x + \phi_m)\,[{a_m}^\dagger(t) - a_m(t)], \tag{C14}$$

with $a(t) = a e^{-i\omega_m t}$ and $k_m = \omega_m/v_0$. The first boundary condition is met by setting $\phi_m = 0$. The second boundary condition gives

$$\tan(k_m l) = \frac{\partial_t Q_m(t)}{\omega_m Q_m(t)}\frac{Z(\omega_m)}{Z_0}, \tag{C15}$$

where $Z_0 = \sqrt{L_0/C}$ is the characteristic impedance of the $\lambda/4$ resonator and $Q_m(t)$ is the time-dependent component of $Q(x,t)$ oscillating at ω_m. The equation must in general be solved numerically for k_m. In the case of an open circuit boundary condition where $Z(\omega) \to i\infty$, we simply have

$$\cos(k_m l) = 0 \Rightarrow k_m = \frac{(2m+1)\pi}{2l} \quad \text{(open)}, \tag{C16a}$$

$$\omega_m = \frac{(2m+1)\pi v_0}{2l}. \tag{C16b}$$

The band-stop filter presents the resonator with a large impedance for frequencies within the stop band. To simplify the following analysis we assume an infinite impedance, that is, an open boundary condition at $x = l$, which allows us to utilize the relations in Eq. (C16).

In the linear case, the canonical momentum is just $\Phi = L_0\dot{Q}$, that is,

$$\Phi(x,t) = -\sum_{m=0}^{\infty} L_0 \omega_m A_m \cos(k_m x)\,[{a_m}^\dagger(t) + a_m(t)]. \tag{C17}$$

Quantization proceeds by imposing the commutation relations $[a_m(t), {a_n}^\dagger(t)] = \delta_{nm}$. The normalization constants A_m are determined by inserting $Q(x,0)$ and $\Phi(x,0)$ into H_{KIPA} and requiring

$$H_0 = \sum_{m=0}^{\infty} \hbar\omega_m \left({a_m}^\dagger a_m + \frac{1}{2} \right), \tag{C18}$$

which leads to $A_m = 1/\sqrt{lL_0\omega_m}$. We therefore find

$$Q(x,t) = i \sum_{m=0}^{\infty} \sqrt{\frac{\hbar}{L_T\omega_m}} \cos(k_m x) \left[{a_m}^\dagger(t) - a_m(t) \right], \tag{C19a}$$

$$\Phi(x,t) = -\frac{1}{l} \sum_{m=0}^{\infty} \sqrt{\hbar L_T \omega_m} \cos(k_m x) \left[{a_m}^\dagger(t) + a_m(t) \right], \tag{C19b}$$

where we define $L_T = L_0 l$ as the total zero-bias kinetic inductance of the resonator.

More generally, we can interpret Eq. (C19) as a change of variables from $\{Q(x,t), \Phi(x,t)\}$ to $\{a_m(t), {a_m}^\dagger(t)\}$, subject to the spatial boundary constraints. Inserting the form of $\Phi(x,t)$ into Eq. (C11c), keeping only the fundamental mode and dropping fast-rotating terms and constants, we find

$$\begin{aligned} H_1 &= -\frac{(\hbar\omega_0)^2}{32 L_T I_*^2} (a^\dagger + a)^4, \\ &\approx -\frac{3(\hbar\omega_0)^2}{16 L_T I_*^2} (2 a^\dagger a + {a^\dagger}^2 a^2), \\ &= \hbar K a^\dagger a + \frac{\hbar K}{2} {a^\dagger}^2 a^2. \end{aligned} \tag{C20}$$

The Kerr nonlinearity is thus

$$K = -\frac{3}{8} \frac{\hbar\omega_0}{L_T I_*^2} \omega_0. \tag{C21}$$

Here $L_T I_*^2/2$ can be interpreted as a characteristic energy stored in an inductor with inductance L_T and current I_*, which is also related to the superconducting pairing energy $E_p \propto L_T I_*^2$ [29].

2. Current bias

a. Mode expansion

In the presence of a current bias, we modify the boundary condition at $x = l$ to be

$$\partial_t Q(x = l) = -\frac{1}{Z(\omega) C} \partial_x Q(x = l) + I_b. \tag{C22}$$

We take the impedance to be a stop-band filter at the relevant resonator mode frequencies:

$$Z_s(\omega) = \begin{cases} i\infty, & \omega \in \Omega_0, \\ 50\ \Omega, & \omega \in \Omega_1, \end{cases} \tag{C23}$$

where Ω_0 represents the frequency band over which we have standing resonator modes, and Ω_1 covers the impedance matched frequency band, where we will have traveling waves. For $I_b = 0$ we can then write

$$\begin{aligned} Q(x,t) = i \sum_m \sqrt{\frac{\hbar}{L_T\omega_m}} \cos(k_m x) \left[{a_m}^\dagger(t) - a_m(t) \right] \\ + i \int_{\Omega_1} d\omega \sqrt{\frac{\hbar}{\pi\omega v_0 L_0}} \cos\left(\frac{\omega x}{v_0}\right) \left[{b_\omega}^\dagger(t) - b_\omega(t) \right], \end{aligned} \tag{C24}$$

with ${b_\omega}^\dagger(t) = {b_\omega}^\dagger e^{i\omega t}$. We already know that the first term satisfies the boundary conditions at frequencies ω_m from our previous analysis, with ω_m, k_m given in Eq. (C16). For frequencies $\omega \in \Omega_1$, on the other hand, the circuit is modeled as a semi-infinite matched transmission line connected to ground at $x = 0$.

In the presence of a current bias, we simply add to $Q(x,t)$ a term $q_b(x,t)$ where $\dot{q}_b(x,t) = I_b(x,t)$. We assume that the pump frequencies are in the traveling-wave band Ω_1. Equivalently, we can replace $b_\omega \to b_\omega + \beta(\omega)$, with $\beta(\omega)$ representing the frequency component of $q_b(t)$ at frequency ω. This can be interpreted as separating the continuum mode into a strong average coherent component $\beta(\omega)$ and a fluctuation (or quantum) term b_ω. We take the pump to be infinitely narrow in frequency, and therefore set $\beta(\omega) = \beta_p \delta(\omega - \omega_p) + \beta_{\mathrm{dc}} \delta(\omega)$. The dc component is independent of space and trivially satisfies both the wave equation Eq. (C12) and the short $\partial_x Q = 0$ boundary condition. We therefore, finally, have

$$\begin{aligned} Q(x,t) = i \sum_m \sqrt{\frac{\hbar}{L_T\omega_m}} \cos(k_m x) \left[{a_m}^\dagger(t) - a_m(t) \right] \\ + i \int_{\Omega_1} d\omega \sqrt{\frac{\hbar}{\pi\omega v_0 L_0}} \cos\left(\frac{\omega x}{v_0}\right) \left[{b_\omega}^\dagger(t) - b_\omega(t) \right] \\ + q_p(x,t) + q_{\mathrm{dc}}(t), \end{aligned} \tag{C25}$$

where:

$$\dot{q}_{\mathrm{dc}}(t) = I_{\mathrm{dc}}, \tag{C26a}$$

$$\dot{q}_p(t) = I_p(x,t) = \cos\left(\frac{\omega_p x}{v_0} + \phi_p\right) I_p(t). \tag{C26b}$$

In our experiments we apply a pump tone $I_p(x,t)$ that oscillates at a frequency very close to $2\omega_0$ and we will

therefore assume $\omega_p = 2\omega_0$ for simplicity. Furthermore, the boundary condition in Eq. (C13a) implies that $\phi_p = 0$. Thus,

$$I_p(x,t) = \cos(2k_0 x) I_p(t). \tag{C27}$$

As before, we will use the strategy of taking the mode expansion of $\Phi(x,t)$ in the absence of any nonlinearity, and substitute this back into the nonlinear Hamiltonian H_1. Using $\Phi(x,t) = L_0 \dot{Q}(x,t)$, we find

$$\begin{aligned}\Phi(x,t) = &-\frac{1}{l}\sum_m \sqrt{\hbar L_T \omega_m}\cos(k_m x)\left[{a_m}^\dagger + a_m\right] \\ &-\frac{1}{v_0}\int_{\Omega_1} d\omega \sqrt{\frac{\hbar\omega Z_0}{\pi}}\cos\left(\frac{\omega x}{v_0}\right)\left[{b_\omega}^\dagger + b_\omega\right] \\ &+ L_0\cos(2k_0 x) I_p(t) + L_0 I_{\rm dc}.\end{aligned} \tag{C28}$$

b. Hamiltonian

For the linear Hamiltonian we have, as before,

$$H_0 = \sum_{m=0}^{\infty} \hbar\omega_m \left({a_m}^\dagger a_m + \frac{1}{2}\right), \tag{C29}$$

where we have kept only the resonator modes and dropped the continuum modes in Ω_1. To proceed we will substitute the (Schrödinger picture) flux field into H_1. In general this will lead to coupling (e.g., cross-Kerr) between resonator and quantum continuum modes. However, given that the nonlinearity of the KIPA is extremely weak, we will neglect the quantum fluctuations of the current, that is, drop the b_ω modes completely from the nonlinearity. We also, for simplicity, truncate to the fundamental resonator mode, and thus use

$$\begin{aligned}\Phi(x,t) = &-\frac{1}{l}\sqrt{\hbar L_T \omega_0}\cos(k_0 x)\left(a^\dagger + a\right) \\ &+ L_0\cos(2k_0 x) I_p(t) + L_0 I_{\rm dc}.\end{aligned} \tag{C30}$$

Dropping fast-rotating terms in a, $a^\dagger$ from H_1, we have

$$\begin{aligned}H_1 = &-\frac{3(\hbar\omega_0)^2}{16 I_*^2 L_T}\left(2a^\dagger a + {a^\dagger}^2 a^2\right) \\ &-\frac{\hbar\omega_0}{8 I_*^2}\left[2I_{\rm dc}^2 + 2I_{\rm dc} I_p(t) + I_p^2(t)\right]\left(2a^\dagger a + {a^\dagger}^2 + a^2\right).\end{aligned} \tag{C31}$$

We take the time-dependent ac current amplitude to be

$$I_p(t) = \frac{I_p}{2}\left(e^{-i(\omega_p t + \varphi_p)} + e^{i(\omega_p t + \varphi_p)}\right). \tag{C32}$$

Substituting $I_p(t)$ into H_1 and transferring to a frame rotating at $\omega_p/2$, the KIPA Hamiltonian becomes

$$\begin{aligned}H_{\rm KIPA} = &\hbar\left(\omega_0 + \delta_{\rm dc} + \delta_p + K - \frac{\omega_p}{2}\right)a^\dagger a \\ &+ \frac{\hbar\xi}{2}{a^\dagger}^2 + \frac{\hbar\xi^*}{2}a^2 + \frac{\hbar K}{2}{a^\dagger}^2 a^2,\end{aligned} \tag{C33}$$

where any fast-rotating pump terms have been ignored. We thus define the following important Hamiltonian parameters:

$$\delta_{\rm dc} = -\frac{1}{2}\frac{I_{\rm dc}^2}{I_*^2}\omega_0, \tag{C34a}$$

$$\delta_p = -\frac{1}{8}\frac{I_p^2}{I_*^2}\omega_0, \tag{C34b}$$

$$K = -\frac{3}{8}\frac{\hbar\omega_0}{L_T I_*^2}\omega_0, \tag{C34c}$$

$$\xi = -\frac{1}{4}\frac{I_{\rm dc} I_p}{I_*^2}\omega_0 e^{-i\varphi_p}. \tag{C34d}$$

We note that the term δ_p arises from the square of the pump current, which has a nonzero average value of $I_p^2/2$ and therefore causes an effective detuning of the cavity frequency.

As a sanity check, in the absence of a pump tone (i.e., $I_p = 0$) we find the resonance frequency of the cavity to be

$$\omega_0' \approx \omega_0\left(1 - \frac{1}{2}\frac{I_{\rm dc}^2}{I_*^2}\right), \tag{C35}$$

neglecting the Kerr term. For $(I_{\rm dc}/I_*)^2 \ll 1$, which is the approximation used in Eq. (C10), we can write

$$\omega_0' \approx \frac{\omega_0}{\sqrt{1 + I_{\rm dc}^2/I_*^2}} = \frac{\pi}{2l\sqrt{C L_k(I_{\rm dc})}}, \tag{C36}$$

which is the fundamental frequency of a $\lambda/4$ resonator with a per-unit length capacitance of C and inductance $L_k(I_{\rm dc})$ [provided by Eq. (C1)], as expected.

3. DPA approximation

A comparison of the expressions for K [Eq. (C34c)] and ξ [Eq. (C34d)] reveals why the KIPA exhibits weak higher-order nonlinearities: the photon energy is a minuscule fraction of the characteristic nonlinear inductive energy [i.e., $\hbar\omega_0/(L_T I_*^2) \ll 1$] by virtue of I_* being large.

Using the per-square kinetic inductance of the film $L_\square = 32$ pH (see Appendix A 3), we find $L_T = L_\square(l/w) = 3.84$ nH (with l and w the length and width of the $\lambda/4$ resonator), which together with the measured value of I_* gives $|K|/2\pi \approx 0.13$ Hz, a completely negligible quantity

relative to all other system parameters. Compared to the coupling rate, we achieve the ratio $\kappa/|K| > 10^8$, greater than the typical values of $\kappa/|K| < 10^4$ seen in JPAs [14]. Because the Kerr term is so small, we approximate the Hamiltonian for the KIPA with the Hamiltonian for the ideal DPA for the remainder of this work:

$$H_{\mathrm{KIPA}} \approx H_{\mathrm{DPA}} = \hbar\Delta a^\dagger a + \frac{\hbar\xi}{2}a^{\dagger 2} + \frac{\hbar\xi^*}{2}a^2, \quad \text{(C37)}$$

with

$$\Delta = \omega_0 + \delta_{\mathrm{dc}} + \delta_p - \omega_p/2, \quad \text{(C38)}$$

which is identical to Eq. (C33) with the Kerr terms neglected.

4. Josephson DPA comparison

To understand why the KIPA is able to closely approximate the DPA Hamiltonian, it is instructive to compare the scaling of the inductance and critical current with that observed in JPAs that exploit SQUID loops. Both a single Josephson junction (JJ) and a kinetic inductance (KI) wire have an inductance expressed as

$$L_{T(J)} = \frac{\hbar R_n}{\pi\Delta_0}, \quad \text{(C39)}$$

where L_T (L_J) is the total kinetic (Josephson) inductance, R_n is the normal state resistance of the KI wire (JJ), and Δ_0 is the superconducting gap energy. The critical current of a JJ is provided by the Ambegaokar-Baratoff formula,

$$I_c = \frac{\pi\Delta_0}{2eR_n}, \quad \text{(C40)}$$

which we can use to rewrite the Josephson inductance as

$$L_J = \left(\frac{\Phi_0}{2\pi}\right)\frac{1}{I_c}, \quad \text{(C41)}$$

where Φ_0 is the superconducting flux quantum. The self-Kerr interaction strength of a JPA with a single SQUID loop is [14,16]

$$K = -\frac{\hbar\omega_0}{8E_J}\omega_0, \quad \text{(C42)}$$

where ω_0 is the amplifier operating frequency and the Josephson energy E_J is written as

$$E_J = \left(\frac{\Phi_0}{2\pi}\right)I_c. \quad \text{(C43)}$$

It is desirable to minimize the Kerr term in a DPA, since it limits the dynamic range and squeezing potential [13–16,38]. This implies that a large E_J and therefore I_c are necessary. Consequently, as a result of Eq. (C41) the Josephson inductance will also be reduced. For a critical current of $I_c = 1$ mA, we find $L_J \approx 0.3$ pH, a value that is approximately two to three orders of magnitude smaller than the geometric inductance in a typical lumped element or distributed resonator at microwave frequencies. This is undesirable, since it has been shown that to minimize the effect of higher-order nonlinearities in the Josephson cosine potential, the Josephson inductance should not be much smaller than the geometric inductance [38].

For a thin KI wire, the nonlinear current (which is proportional to the critical current) can be estimated from Mattis-Bardeen theory [29] and is given by

$$I_* = \sqrt{\frac{\pi N_0\Delta_0^3 V}{\hbar R_n}}, \quad \text{(C44)}$$

where N_0 is the single-spin density of electron states at the Fermi energy and V is the volume of the wire. This relation holds in the limit that the film is thin compared to its penetration depth, which is true for our 9.5-nm-thick $Nb_xTi_{1-x}N$ film. From Eq. (C44) it is becomes evident that one can control the current nonlinearity in a KI wire independently of its inductance. Increasing both the cross-sectional area A and the length l of the wire by a factor α raises the volume $V = Al$ by an amount α^2, but leaves the normal state resistance $R_n = \rho_n l/A$ (with ρ_n the resistivity) unchanged. This in turn leaves the kinetic inductance L_T unchanged. A wire of width $w = 0.1$ μm and length $l = 10$ μm has the same kinetic inductance as a wire of width $w = 10$ μm and length $l = 1000$ μm, but a nonlinear current I_* that is two orders of magnitude smaller. In our resonator we achieve $I_* \approx 5$ mA with $L_T = 3.84$ nH, an inductance more than four orders of magnitude larger than what would be accessible using a single JJ with an equivalent critical current. We have summarized the nonlinear current, inductance, energy, and self-Kerr dependencies for a single SQUID JJ device and a KI wire in Table I.

Instead of increasing the critical current in a JPA with a single SQUID loop, the common approach is to use an

TABLE I. Comparison of the nonlinear current, inductance, energy, and Kerr interaction strength for a single SQUID loop JJ device and a KI wire.

Josephson junction	Kinetic inductance
$I_c = \frac{\pi\Delta_0}{2eR_n}$	$I_* = \sqrt{\frac{\pi N_0\Delta_0^3 V}{\hbar R_n}}$
$L_J = \frac{\Phi_0}{2\pi}\frac{1}{I_c} = \frac{\hbar R_n}{\pi\Delta_0}$	$L_T = \frac{\hbar R_n}{\pi\Delta_0}$
$E_J = \frac{\Phi_0}{2\pi}I_c$	$E_p = 2N_0\Delta_0^2 V$
$K = -\frac{\hbar\omega_0}{8E_J}\omega_0 = -\frac{\hbar\omega_0}{8L_J I_c^2}\omega_0$	$K = -\frac{3\hbar\omega_0}{8E_p}\omega_0 = -\frac{3\hbar\omega_0}{4L_T I_*^2}\omega_0$

array of N SQUIDs, each with a critical current NI_c, energy NE_J, and inductance L_J/N. The total inductance of the array remains L_J, but the self-Kerr strength of the array is reduced by a factor N^2 relative to a single SQUID with a critical current I_c [15,38]. As discussed in Ref. [38], in practice this is difficult to implement, since not all SQUID loops will have an identical Josephson energy (due to fabrication imperfections and inhomogeneous coupling to the flux line), and, as further noted in Ref. [16], the validity of the assumptions that lead to the N^2 reduction in the Kerr term breaks down when the SQUID array approaches the size of the wavelength.

An equivalent picture can be formed for the KI wire by equating the nonlinear kinetic inductance energy with the superconducting pairing energy $E_p \propto L_T I_*^2$ [29], which itself depends on the effective volume of the inductance (see Table I). Since $|K| \propto 1/E_p$, as the volume over which L_T is spread gets larger, the self-Kerr interaction gets smaller. This is in a sense analogous to the use of SQUID arrays in JPAs, where, as noted, distributing many weakly nonlinear SQUIDs throughout the resonator can substantially lower the self-Kerr interaction strength relative to the case of a single SQUID [38]. It is interesting to note that if we fix the length of the wire and only vary its area, then a similar scaling to the Josephson junction is expected, where an increase in the nonlinear current is accompanied by a reduction in the inductance by the same factor (i.e., $L_T \propto 1/I_*$).

APPENDIX D: INPUT-OUTPUT THEORY FOR A DPA

The field operators a, Φ, and Q and Hamiltonian H_{KIPA} so far describe the intracavity field dynamics. In the experimental setting we stimulate the resonator with an input field operator a_{in} and measure a reflected response a_{out} that enter and exit the cavity via the coupling circuit. For example, a vector network analyzer measures the reflection parameter $S_{11}(\omega) = \langle a_{\mathrm{in}}\rangle/\langle a_{\mathrm{out}}\rangle$. To obtain a classical description of the microwave response we would typically adopt a scattering matrix approach [58]. The derivation below follows that presented in Ref. [61], and is reproduced here for completeness.

Input-output theory, developed by Gardiner and Collett [62], extends the scattering matrix formalism to the quantum regime. Let H be the Hamiltonian written in terms of the creation and annihilation operators $a^\dagger$ and a, where H is coupled to the bath at rate γ, used to model the losses in the system, and input field a_{in} at rate κ (see Fig. 9). We write down the following Heisenberg picture master equation to describe the system:

$$\frac{\partial a(t)}{\partial t} = \frac{[a(t), H]}{i\hbar} - \bar{\kappa} a(t) + \sqrt{\kappa} a_{\mathrm{in}}(t) + \sqrt{\gamma} b_{\mathrm{in}}(t), \tag{D1}$$

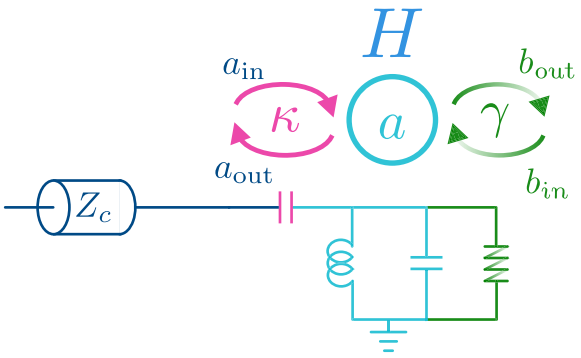

FIG. 9. The single-port input-output theory system, with input and output fields a_{in} and a_{out}, intracavity field operator a, and bath input and output fields b_{in} and b_{out}. The input field is coupled to the cavity at rate κ, and the cavity to the bath at rate γ. The accompanying circuit is colored according to the correspondence with the associated fields and coupling constants. The bath continuum is coupled to the circuit via the resistor.

where $\bar{\kappa} = (\gamma + \kappa)/2$ and b_{in} is the bath input field operator. The output field operator a_{out} is then given by the input-output relation

$$a_{\mathrm{out}}(t) + a_{\mathrm{in}}(t) = \sqrt{\kappa} a(t). \tag{D2}$$

Consider now the linear $\lambda/4$ resonator Hamiltonian provided in Eq. (C18), truncated to the fundamental mode. We rewrite Eq. (D1) in the Fourier domain using

$$a[\omega] = \frac{1}{\sqrt{2\pi}} \int_{-\infty}^{\infty} e^{i\omega t} a(t) d\omega, \tag{D3}$$

which gives

$$\begin{aligned} -i\omega a[\omega] &= -\frac{i}{\hbar}\left(a[\omega], \hbar\omega_0 a^\dagger[\omega] a[\omega]\right) - \bar{\kappa} a[\omega] \\ &\quad + \sqrt{\kappa} a_{\mathrm{in}}[\omega] + \sqrt{\gamma} b_{\mathrm{in}}[\omega] \\ -i\omega a &= -i\omega_0 a - \bar{\kappa} a + \sqrt{\kappa} a_{\mathrm{in}} + \sqrt{\gamma} b_{\mathrm{in}}. \end{aligned} \tag{D4}$$

Substituting for a using the input-output relation [Eq. (D2)] yields the output field operator in terms of the input and bath fields:

$$\begin{aligned} -i\omega(a_{\mathrm{out}} + a_{\mathrm{in}}) &= -(\bar{\kappa} + i\omega_0)(a_{\mathrm{out}} + a_{\mathrm{in}}) \\ &\quad + \kappa a_{\mathrm{in}} + \sqrt{\gamma\kappa} b_{\mathrm{in}} \\ \Rightarrow a_{\mathrm{out}} &= \left(\frac{\kappa}{\bar{\kappa} - i(\omega - \omega_0)} - 1\right) a_{\mathrm{in}} \\ &\quad + \frac{\sqrt{\gamma\kappa}}{\bar{\kappa} - i(\omega - \omega_0)} b_{\mathrm{in}}. \end{aligned} \tag{D5}$$

Treating the bath input field b_{in} as a thermal state such that $\langle b_{\mathrm{in}}\rangle = 0$, we retrieve the expression for the reflection

parameter:

$$S_{11}[\omega] = \frac{\langle a_{\text{out}}[\omega]\rangle}{\langle a_{\text{in}}[\omega]\rangle} \tag{D6}$$

$$= \frac{\kappa}{\bar{\kappa} - i(\omega - \omega_0)} - 1. \tag{D7}$$

We can apply the same mathematics to the idealized KIPA Hamiltonian [Eq. (C37)]. We first write the master equation in the Fourier domain, as before [14]:

$$-i\omega a = -\left(\bar{\kappa} a + i\Delta a + i\frac{\xi}{2}\left[a, a^{\dagger 2}\right] + i\frac{\xi^*}{2}\left[a, a^2\right]\right) + \sqrt{\kappa} a_{\text{in}} + \sqrt{\gamma} b_{\text{in}},$$

$$-i\omega a = -[(\bar{\kappa} + i\Delta)a + i\xi a^\dagger] + \sqrt{\kappa} a_{\text{in}} + \sqrt{\gamma} b_{\text{in}}. \tag{D8}$$

Next, we take the Hermitian conjugate of both sides. Note that in the Fourier domain $(a[\omega])^\dagger = a^\dagger[-\omega]$. To simplify notation the frequency reversal is implied. We find

$$i\omega a^\dagger = -[(\bar{\kappa} - i\Delta)a^\dagger - i\xi^* a] + \sqrt{\kappa} a_{\text{in}}^\dagger + \sqrt{\gamma} b_{\text{in}}^\dagger. \tag{D9}$$

Combined with Eq. (D8), we obtain the matrix equation

$$i\omega \begin{pmatrix} -a \\ a^\dagger \end{pmatrix} = \begin{pmatrix} -i\Delta - \bar{\kappa} & -i\xi \\ i\xi^* & i\Delta - \bar{\kappa} \end{pmatrix} \begin{pmatrix} a \\ a^\dagger \end{pmatrix} + \sqrt{\kappa} \begin{pmatrix} a_{\text{in}} \\ a_{\text{in}}^\dagger \end{pmatrix} + \sqrt{\gamma} \begin{pmatrix} b_{\text{in}} \\ b_{\text{in}}^\dagger \end{pmatrix}$$

$$\Rightarrow \begin{pmatrix} a \\ a^\dagger \end{pmatrix} = -\sqrt{\kappa} \begin{pmatrix} -i\Delta + \bar{\kappa} + i\omega & -i\xi \\ i\xi^* & i\Delta - \bar{\kappa} - i\omega \end{pmatrix}^{-1} \left[\begin{pmatrix} a_{\text{in}} \\ a_{\text{in}}^\dagger \end{pmatrix} + \sqrt{\frac{\gamma}{\kappa}} \begin{pmatrix} b_{\text{in}} \\ b_{\text{in}}^\dagger \end{pmatrix} \right]$$

$$= -\frac{\sqrt{\kappa}}{D[\omega]} \begin{pmatrix} -i\Delta + \bar{\kappa} + i\omega & -i\xi \\ i\xi^* & i\Delta - \bar{\kappa} - i\omega \end{pmatrix} \left[\begin{pmatrix} a_{\text{in}} \\ a_{\text{in}}^\dagger \end{pmatrix} + \sqrt{\frac{\gamma}{\kappa}} \begin{pmatrix} b_{\text{in}} \\ b_{\text{in}}^\dagger \end{pmatrix} \right], \tag{D10}$$

where $D[\omega] = \Delta^2 + (\bar{\kappa} - i\omega)^2 - |\xi|^2$. Substituting the input-output relation Eq. (D2) gives the input-output equation for the ideal DPA [14],

$$a_{\text{out}}[\omega] = g_S[\omega] a_{\text{in}}[\omega] + g_I[\omega] a_{\text{in}}^\dagger[-\omega] + \sqrt{\frac{\gamma}{\kappa}}\left[(g_S[\omega] + 1) b_{\text{in}}[\omega] + g_I[\omega] b_{\text{in}}^\dagger[-\omega]\right], \tag{D11}$$

where we make the frequency reversal explicit, and define the signal and idler gains

$$g_S[\omega] = \frac{\kappa\bar{\kappa} - i\kappa(\Delta + \omega)}{D[\omega]} - 1, \qquad g_I[\omega] = \frac{-i\xi\kappa}{D[\omega]}. \tag{D12}$$

APPENDIX E: PHASE-INSENSITIVE AMPLIFICATION

Phase-insensitive gain is readily measured with a vector network analyzer once an appropriate pump tone and bias current are applied to the device concurrently. For the measurements in Fig. 2(a), we chose a pump frequency of $\omega_p/2\pi = 14.381$ GHz $\approx \omega_0/\pi$, close to twice the resonant frequency of $\omega_0/2\pi = 7.1924$ GHz for the bias current $I_{\text{dc}} = 0.834$ mA. Ideally, the KIPA should be operated at precisely $\Delta = 0$, or $\omega_p \approx 2(\omega_0 + \delta_{\text{dc}} + \delta_p)$ for maximal gain. However, in our experiments we optimize the pump frequency for gain at a fixed pump power and bias current, arriving at a pump configuration close to optimal. A fixed pump frequency of $\omega_p/2\pi = 14.381$ GHz is used throughout the experiments, despite the expected shift in resonance [Eq. (C34)].

The VNA supplies a signal tone, which is swept about $\omega_p/2$, while the reflected response from the KIPA is measured. Because the magnitude response of the KIPA is approximately flat, we measure gain by taking the difference between the response with the pump on and the pump off, depicted in Fig. 2 at different pump powers. The KIPA produces an amplified signal tone ω_s at its output, along with an idler at ω_i such that energy is conserved in the 3WM process, $\omega_p = \omega_s + \omega_i$. Phase-insensitive gain occurs when $\omega_s = \omega_p/2 + \Delta\omega$ with $|\Delta\omega|$ exceeding the bandwidth resolution of the measurement. Gain increases with the pump power and is found to be in excess of 40 dB before the KIPA crosses the threshold where spontaneous parametric oscillations occur (see Appendix E 3).

1. Gain feature fits

To characterize the line-shape of the nondegenerate amplification features in the main text, we define the reflection parameter $\Gamma(\omega)$, which is simply the signal gain [Eq. (D12)] written in the laboratory frame (i.e., $g_S[\omega] \to \Gamma(\omega)$ with $\omega \to \omega - \omega_p/2$) [14]:

$$\Gamma(\omega) = \frac{\kappa(\kappa+\gamma)/2 + i\kappa(\Delta+\omega-\omega_p/2)}{\Delta^2 + \left[(\kappa+\gamma)/2 + i(\omega-\omega_p/2)\right]^2 - |\xi|^2} - 1. \tag{E1}$$

To fit the data in Fig. 2, we adopt a complex coupling rate in the reflection model $\Gamma(\omega)$: $\kappa \in \mathbb{R} \to \kappa \in \mathbb{C}$, with complex phase $\mathrm{Arg}(\kappa)$. A complex quality factor may be used to model an asymmetric response that occurs due to an impedance mismatch across the coupling circuit where reflections at the coupler interfere with photons exiting the resonator [63,64].

The pump current in our device is not precisely known. We simulate an impedance of $Z_0 = 118\ \Omega$ for the $\lambda/4$ resonator (using the software Sonnet) and introduce a loss parameter λ_p that quantifies the amount of pump power transmitted from room temperature down to the sample such that $I_p^2 = 2\lambda_p P_{\mathrm{pump}}/Z_0$, where P_{pump} is the pump power at the microwave source.

We may predict the parameter $\Delta = \omega_0 + \delta_{\mathrm{dc}} + \delta_p - \omega_p/2$ from our theory [Eqs. (C34a) and (C34b)] as ω_p and I_{dc} are known, and we have measured ω_0 and I_*. Further, Eq. (C34d) allows us also to predict $|\xi|$ as a function of the pump current in the sample. To further constrain the model we assume the quality factor $Q_i = \omega_0/\gamma$ to be 10^5 for all pump powers. We base this estimate on the internal quality factors observed in similar devices (e.g., the device measured in Fig. 23), and note that in the overcoupled regime in which the KIPA operates Q_i has minimal impact on the predicted gain as $\kappa + \gamma \approx \kappa$. We are left with a model where the only free parameters are $|\kappa|$, $\mathrm{Arg}(\kappa)$ and λ_p. The fit results are shown in Fig. 10.

We observe that κ varies from approximately 52 MHz to approximately 54 MHz, corresponding to an average coupling quality factor of $Q_c \approx 135$. The root-mean-square pump current increases the kinetic inductance and thus modifies the coupling circuit (i.e., it changes the impedance step in the band-stop filter), which might explain the pump-power-dependent coupling rate κ. A weak drift (approximately 30 mrad) in the phase of the coupling rate was necessary to fit the data [see Fig. 10(c)].

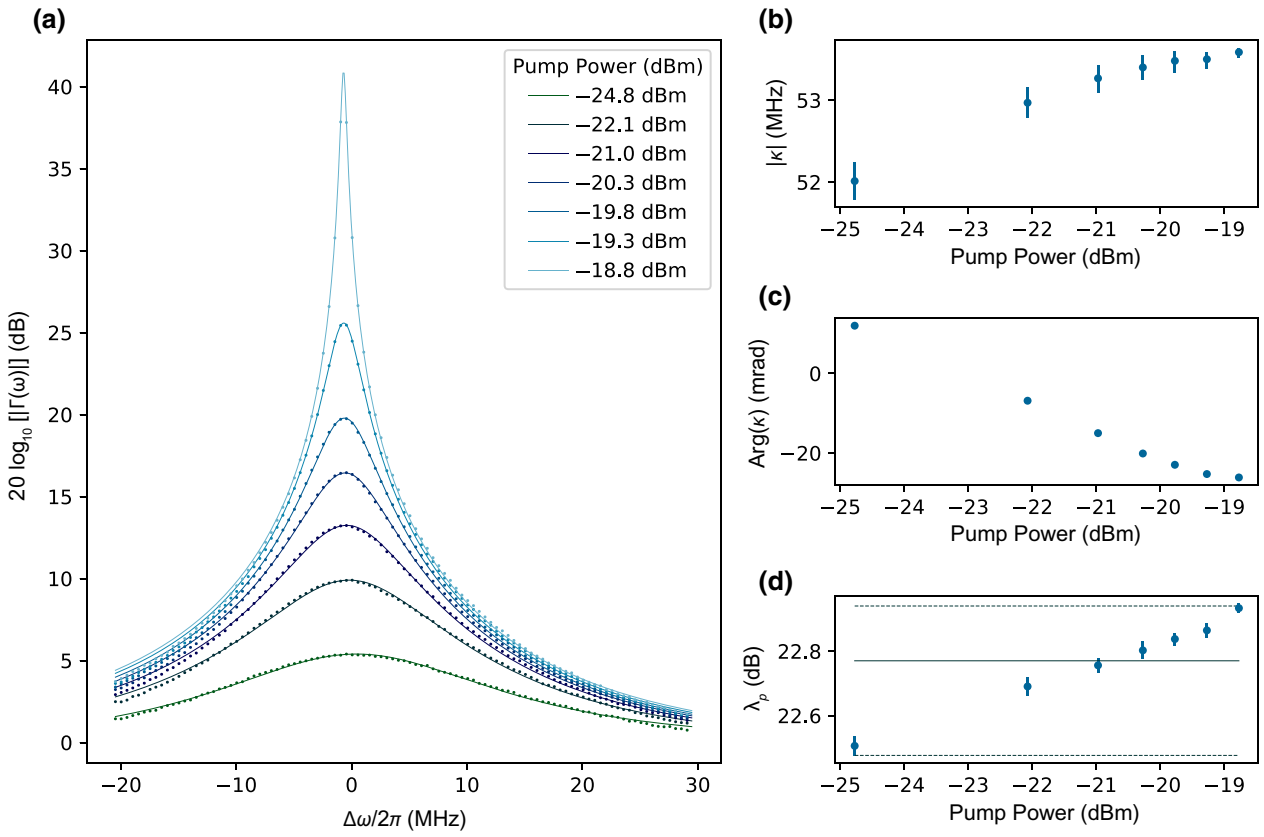

FIG. 10. (a) Phase-insensitive gain as a function of frequency $\omega = \Delta\omega + \omega_p/2$ for different pump powers (circles). Traces are labeled by the pump power at the cavity input. The fitted theoretical frequency response is plotted (solid lines). The parameters $|\kappa|$, $\mathrm{Arg}(\kappa)$, and the pump line transmittance λ_p were the only free parameters. (b) $|\kappa|$ as a function of the estimated pump current in the device (circles). (c) $\mathrm{Arg}(\kappa)$ as a function of pump power. (c) Pump transmittance λ_p as a function of pump power.

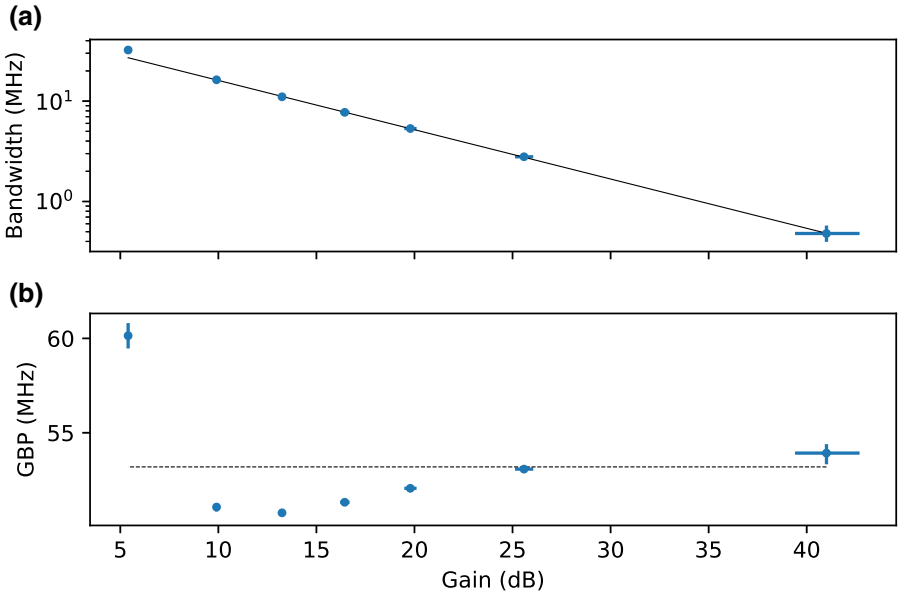

FIG. 11. (a) Bandwidth versus peak phase-insensitive gain. The solid black line is a log-linear fit to the bandwidth as a function of gain in decibels. (b) Gain-bandwidth product (GBP) versus peak phase-insensitive gain (bottom). The dashed black line is the average GBP across all gains.

This is not unreasonable, as a small shift in the cavity and coupling circuit impedances due to the pump current will influence any reflections that occur at the cavity input.

From the fits, we extract an average pump attenuation of $-10\log(\lambda_p) = 22.8$ dB. At room temperature the measured loss of the lines and components is approximately 30 dB. Since the line and component loss is expected to reduce at cryogenic temperatures, this fitted average pump attenuation is realistic. We also note that the extracted pump attenuation increases marginally as the pump power increases, rising by approximately 0.4 dB over the range of powers explored [see Fig. 10(d)]. This could be an indication that the pump becomes slightly depleted as the gain rises [19].

Overall, we find excellent quantitative agreement with our theory, and are able to predict the observed gain curves from the KIPA Hamiltonian [Eqs. (C33)–(C34)] derived in Appendix C.

2. Gain-bandwidth product

From the fits to the amplification features depicted in Fig. 10, we can extract the gain-bandwidth product (GBP), defined by the product of the peak phase-insensitive amplitude gain G and the bandwidth when the amplitude gain drops to $G/\sqrt{2}$ [15]. We find that the GBP of the KIPA shows good consistency across the different pump powers, as evidenced by the highly linear log-log plot of the gain and bandwidth (see Fig. 11), and we extract an average GBP of 53(7) MHz.

3. Parametric self-oscillations

Increasing the pump current I_p, and hence ξ, will not increase the gain indefinitely. Past a certain threshold, the device enters the regime of parametric self-oscillation and ceases to behave as an amplifier [65]. Pumped at twice the resonant frequency, the cavity spontaneously produces photons at ω_0 that grow rapidly in number. Competition from system nonlinearities eventually limits growth, resulting in a fixed power ω_0 tone at steady state.

Although we do not study the KIPA in the self-oscillation regime in this work, we use our theory to predict the range of pump currents at which the KIPA behaves as a parametric amplifier. The parametric oscillation threshold corresponds to the zero crossing of the denominator of $|\Gamma(\omega)|$. At the point of maximum phase-sensitive amplification, spontaneous oscillations occur when $|\xi|^2 \geq \Delta^2 + (\kappa+\gamma)^2/4$. Using our theory along with the coupling rate $|\kappa|$ extracted from the fits depicted in Fig. 10, we can predict the pump current at which parametric self-oscillation occurs. We assume a real coupling rate κ to simplify the analysis.

Figure 12 depicts the predicted $|\xi|$ as a function of pump power alongside the predicted threshold of parametric self-oscillation: $\sqrt{\Delta^2 + (\kappa+\gamma)^2/4}$. The threshold increases with the pump power due to the pump-dependent detuning δ_p, which increases Δ^2 as the pump current becomes larger. The curves intersect at a pump power of $P_{\text{pump}} = 4.22$ dBm referred to the output of our microwave source.

We found in practice that the KIPA would self-oscillate beyond a pump power of 4.10 dBm, demonstrating an excellent quantitative agreement between experiment and theory.

APPENDIX F: PHASE-SENSITIVE AMPLIFICATION

1. Phase-sensitive gain

When applying a signal tone at half the pump frequency $\omega_s = \omega_p/2$, the KIPA enters the degenerate mode of

operation, producing phase-sensitive gain as the signal and idler tones interfere. From the input-output equations [see Eq. (D12)], the rotating-frame gain is $\Gamma(\varphi_p) = g_S[0] + g_I[0]$. More explicitly, the phase-sensitive gain is

$$|\Gamma(\varphi_p)| = \left|\frac{\kappa(\kappa+\gamma)/2 + i\kappa\Delta + i\kappa|\xi|e^{-j\varphi_p}}{\Delta^2 + (\kappa+\gamma)^2/4 - |\xi^2|} - 1\right|$$
$$= \sqrt{\left[\frac{\kappa[(\kappa+\gamma)/2 - |\xi|\sin(\varphi_p)]}{\Delta^2 + (\kappa+\gamma)^2/4 - |\xi|^2} - 1\right]^2 + \left[\frac{\kappa[\Delta + |\xi|\cos(\varphi_p)]}{\Delta^2 + (\kappa+\gamma)^2/4 - |\xi|^2}\right]^2}, \quad \text{(F1)}$$

where we separate out the modulus of ξ and its argument corresponding to the pump phase φ_p [see Eq. (C34d)]. From Eq. (F1) we observe that the KIPA gain is sensitive to the pump phase φ_p.

Experimentally, we observe phase-sensitive amplification by modulating the phase of a signal tone which has a frequency of $\omega_p/4\pi = 7.1905$ GHz. As φ_p represents the phase difference between the signal and the pump, phase modulation of either tone will allow us to characterize the phase-sensitive gain. Figure 2(b) of the main text [reproduced here in Fig. 13(a)] depicts the gain of the KIPA as a function of pump phase, where up to 26 dB of deamplification and close to 50 dB of amplification are observed. Compared to phase-insensitive amplification, additional gain is observed in degenerate mode due to the constructive interference that occurs between the signal and idler. The traces are aligned such that the point of maximum deamplification occurs for $\varphi_p = 0$.

Figure 13(b) shows the phase-sensitive gain predicted by our theory [Eq. (F1)], where we use interpolated data from the fitted κ points in Fig. 10, the extracted pump loss

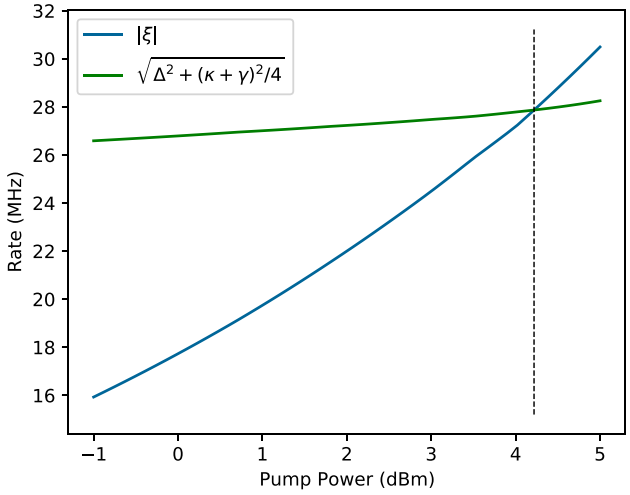

FIG. 12. The rate $|\xi|$ and parametric self-oscillation threshold $\sqrt{\Delta^2 + (\kappa+\gamma)^2/4}$ versus the pump power at the microwave source output. The parametric self-oscillation threshold occurs at the intersection of these curves indicated by the black dashed line at $P_{\text{pump}} = 4.22$ dBm.

$\lambda_p = 22.8$ dB, and the pump-current-dependent expressions for ξ and $\delta\omega$ from our Hamiltonian derivation (Appendix C). We find excellent agreement with theory for the amplification regions of each pump power. On the other hand, the theory predicts greater deamplification than is observed experimentally for the three highest pump powers. To obtain the data plotted in Fig. 13(a), significant averaging was required to reduce the noise. We believe that the maximum deamplification of 26 dB measured is partially limited by our ability to resolve the sharp gain feature at $\varphi_p = 0$, which is highly sensitive to instrumental phase noise and slow phase drifts between the signal and pump. Reflections may also limit the observed deamplification, as discussed in Appendix G.

2. One-decibel compression point

The 1-dB compression point of the KIPA is characterized in phase-sensitive mode. After calibrating the phase of the pump to achieve maximum amplification (i.e., $\varphi_p \approx \pi/2$), we characterize the degenerate 1-dB compression point of the KIPA by increasing the signal power until the gain drops by 1 dB, as is presented in Fig. 2(c). For approximately 20 dB of phase-sensitive gain, we find a compression power of $-49.5(8)$ dBm at the KIPA output, comparable to the compression performance of kinetic inductance traveling-wave amplifiers [23,24,27]. Our HEMT is expected to saturate for input powers of approximately -46 dBm [66]. Factoring in the loss between the KIPA and the HEMT, we are unable to rule out the possibility that the measured the 1-dB compression point is limited by the HEMT, and that the dynamic range of the KIPA is indeed higher.

APPENDIX G: PHASOR TRANSFORMATION OF THE DPA

1. The phasor transformation

Rewriting the input-output relation [Eq. (D11)] in the degenerate case ($\omega = 0$), we find [14]

$$a_{\text{out}} = g_s a_{\text{in}} + g_i a_{\text{in}}^\dagger + \sqrt{\frac{\gamma}{\kappa}}\left[(g_s+1)b_{\text{in}} + g_i b_{\text{in}}^\dagger\right], \quad \text{(G1)}$$

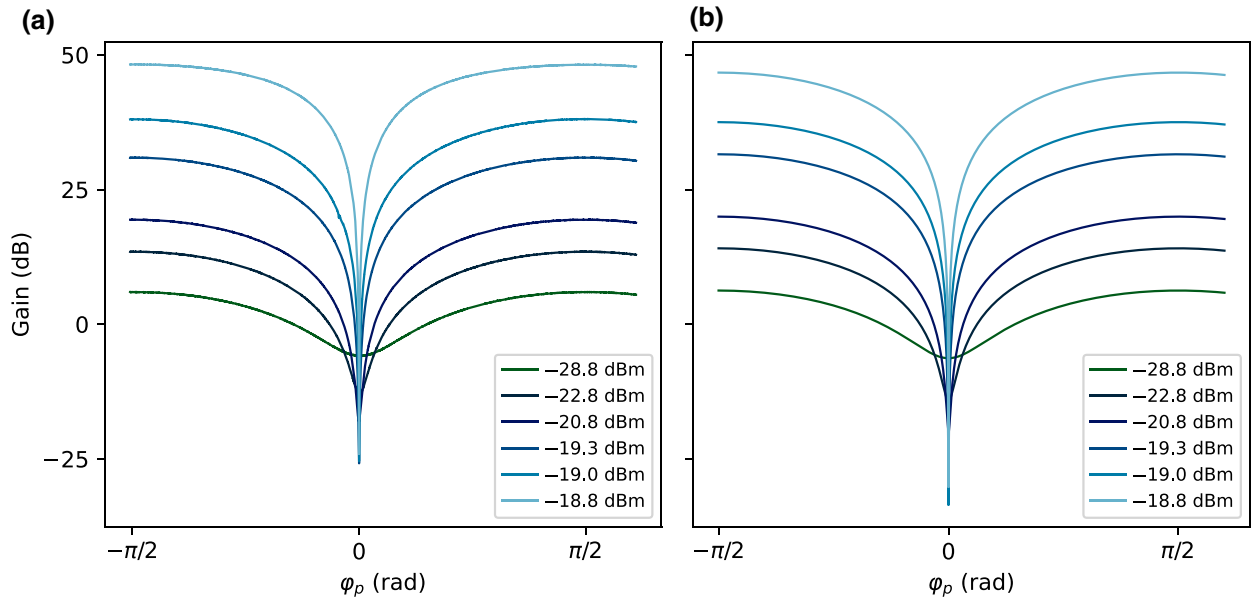

FIG. 13. (a) Measured gain and (b) theoretical gain as a function of the relative pump and signal phase for an input signal of frequency $\omega_s = \omega_p/2$. Traces are labeled by the pump power at the device input (see legend). A slight discrepancy between theory and experiment at the highest pump power (−18.8 dBm) is due to an increasing sensitivity of the peak theoretical gain to coupling rate $|\kappa|$.

$$a_{\text{out}}^\dagger = g_s^* a_{\text{in}}^\dagger + g_i^* a_{\text{in}} + \sqrt{\frac{\gamma}{\kappa}}\left[(g_s^*+1)b_{\text{in}}^\dagger + g_i^* b_{\text{in}}\right], \quad \text{(G2)}$$

giving the output quadrature relations

$$\begin{aligned} I_{\text{out}} &= \frac{1}{2}(a_{\text{out}}^\dagger + a_{\text{out}}) \\ &= \frac{1}{2}\left[\epsilon a_{\text{in}} + \epsilon^* a_{\text{in}}^\dagger + \sqrt{\frac{\gamma}{\kappa}}\left[(\epsilon+1)b_{\text{in}} + (\epsilon^*+1)b_{\text{in}}^\dagger\right]\right] \end{aligned} \quad \text{(G3)}$$

$$\begin{aligned} Q_{\text{out}} &= \frac{i}{2}(a_{\text{out}}^\dagger - a_{\text{out}}) \\ &= \frac{i}{2}\left[\epsilon'^* a_{\text{in}}^\dagger - \epsilon' a_{\text{in}} + \sqrt{\frac{\gamma}{\kappa}}\left[(\epsilon'^*+1)b_{\text{in}}^\dagger - (\epsilon'+1)b_{\text{in}}\right]\right] \end{aligned} \quad \text{(G4)}$$

where $\epsilon = g_s + g_i^*$ and $\epsilon' = g_s - g_i^*$. Using the identities

$$\frac{1}{2}\left[\beta^* a^\dagger + \beta a\right] = \text{Re}(\beta) I - \text{Im}(\beta) Q, \quad \text{(G5)}$$

$$\frac{i}{2}\left[\beta^* a^\dagger - \beta a\right] = \text{Re}(\beta) Q + \text{Im}(\beta) I, \quad \text{(G6)}$$

where β is an arbitrary complex number (such as ϵ or ϵ'), we arrive at a set of linear equations for the output field quadratures:

$$\begin{pmatrix} I_{\text{out}} \\ Q_{\text{out}} \end{pmatrix} = A_G \begin{pmatrix} I_{\text{in}} \\ Q_{\text{in}} \end{pmatrix} + \sqrt{\frac{\gamma}{\kappa}}(A_G + 1)\begin{pmatrix} I_b \\ Q_b \end{pmatrix}, \quad \text{(G7)}$$

where I_b and Q_b are the quadrature operators of the bath field. As a function of the pump phase φ_p, the affine transformation of the quadratures A_G is given by

$$\begin{aligned} A_G(\varphi_p) &= \begin{pmatrix} \text{Re}(\epsilon) & -\text{Im}(\epsilon) \\ \text{Im}(\epsilon') & \text{Re}(\epsilon') \end{pmatrix} \\ &= \frac{\kappa}{\Delta^2 + (\kappa+\gamma)^2/4 - |\xi|^2}\begin{pmatrix} (\kappa+\gamma)/2 - |\xi|\sin(\varphi_p) & -|\xi|\cos(\varphi_p) + \Delta \\ -|\xi|\cos(\varphi_p) - \Delta & (\kappa+\gamma)/2 + |\xi|\sin(\varphi_p) \end{pmatrix} - 1. \end{aligned} \quad \text{(G8)}$$

The pump phase φ_p has the effect of rotating the basis of the transformation. In fact, one can show that $A_G(\varphi_p) = R^T(\varphi_p) A_G(0) R(\varphi_p)$ where $R(\theta)$ is the standard 2×2 rotation matrix.

As the bath is a thermal state, taking the expectation of both sides of Eq. (G7) gives the simple expression

$$\begin{pmatrix} \langle I_{\text{out}} \rangle \\ \langle Q_{\text{out}} \rangle \end{pmatrix} = A_G(\varphi_p) \begin{pmatrix} \langle I_{\text{in}} \rangle \\ \langle Q_{\text{in}} \rangle \end{pmatrix}. \tag{G9}$$

Assuming $\Delta = 0$ we find $A_G \to 1$ in the limit that $|\xi| \to 0$, as expected. Conversely, if $\Delta \neq 0$ then A_G is an affine transformation that will always mix the input quadratures to some degree, limiting the achievable squeezing for a given ξ. Figure 14 illustrates the mapping of points on the unit circle $(I, Q)^T = [\sin(\phi), \cos(\phi)]^T$ in the vector space $V \in \mathbb{R}^2$ by the linear transformation $A_G(0) : V \to W$. Setting $\varphi_p = 0$ yields a mapping where the standard unit vectors in V do not in general map to the standard unit vectors in W, nor do they correspond to the principal axes of the elliptical output state.

We may align the axis of amplification along Q, as depicted in Fig. 15, by choosing $\varphi_p = \pi/2 - \arccos(-\Delta/|\xi|)$. Note that in Fig. 15 we deliberately set $\Delta \neq 0$ to illustrate the fact that orthogonal vectors in V do not necessarily map to orthogonal vectors in W. On the other hand, when $\Delta = 0$, the optimal angle of rotation will correspond to $\varphi_p = 3\pi/2$, giving a strictly diagonal matrix $A_G(\varphi_p)$ with partial diagonal elements $(\kappa + \gamma)/2 + |\xi|$ and $(\kappa + \gamma)/2 - |\xi|$, such that orthogonality is preserved. Degenerate amplification increases as $|\xi|$ approaches the asymptote of self-oscillation $[|\xi|^2 = \Delta^2 + (\kappa + \gamma)^2/4]$, while simultaneously deamplification approaches 0.

The expression for gain as a function of the pump phase φ_p is given by

$$g(\varphi_p) = \frac{||(\langle I_{\text{out}} \rangle, \langle Q_{\text{out}} \rangle)^T||}{||(\langle I_{\text{in}} \rangle, \langle Q_{\text{in}} \rangle)^T||} = \sqrt{\frac{[\langle I_{\text{in}} \rangle g_{11}(\varphi_p) + \langle Q_{\text{in}} \rangle g_{12}(\varphi_p)]^2 + [\langle I_{\text{in}} \rangle g_{21}(\varphi_p) + \langle Q_{\text{in}} \rangle g_{22}(\varphi_p)]^2}{\langle I_{\text{in}} \rangle^2 + \langle Q_{\text{in}} \rangle^2}}, \tag{G10}$$

where g_{ij} are the matrix elements of $A_G(\varphi_p)$. This corresponds exactly with the expression for phase-sensitive gain provided earlier in Eq. (F1).

2. Reflections with the predicted phasor transformation

The ellipses depicted in Fig. 3 are not simply a result of the phasor transformation applied to coherent inputs of fixed magnitude. Because our setup is not perfectly impedance- matched, reflections will occur at the input to the KIPA (e.g., from the PCB and input connector) that superimpose on the phasor transformation. Although these reflections only account for a small percentage of the detected signal, they become considerable as the deamplification increases.

To be precise, we define "reflections" to be the total microwave signal that propagates towards the HEMT input that has not been amplified by the KIPA. The total reflected

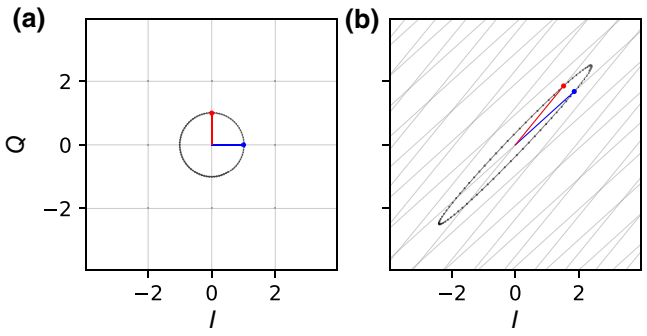

FIG. 14. Visualization of the linear transformation $A_G(0)$ acting on points on the unit circle. The red (blue) points/lines correspond to the standard basis vectors in V. (a) Unit circle before the transformation $A_G(0)$. (b) Unit circle after the transformation.

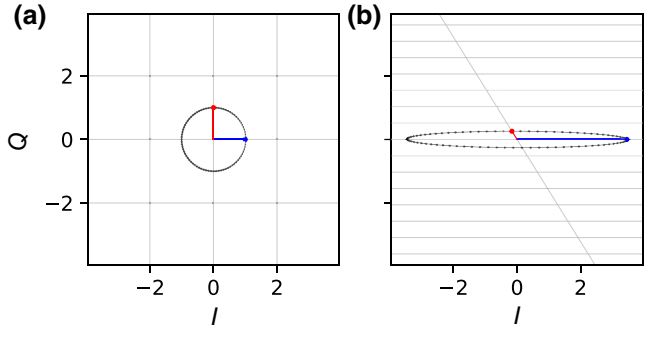

FIG. 15. Visualization of the linear transformation $A_G[\pi/2 - \arccos(-\Delta/|\xi|)]$ acting on points on the unit circle. The red (blue) points and lines correspond to the standard basis vectors in V. (a) Unit circle before the transformation $A_G[\pi/2 - \arccos(-\Delta/|\xi|)]$. (b) Unit circle after the transformation.

signal will have a constant amplitude that is a fraction of the input amplitude, and, relative to the KIPA output, will be offset in phase according to the difference in path length. Taking the vector sum between the total reflected signal and the phase-sensitive output of the KIPA gives a resulting ellipse that we observe at the output of our fridge (see Fig. 16). That is,

$$\begin{pmatrix} \langle I_{\text{out}} \rangle \\ \langle Q_{\text{out}} \rangle \end{pmatrix} = \left[\mathcal{T} A_G(\varphi_p) + \mathcal{R} R(\phi) \right] \begin{pmatrix} \langle I_{\text{in}} \rangle \\ \langle Q_{\text{in}} \rangle \end{pmatrix}, \quad \text{(G11)}$$

where $\mathcal{T}$ is the coefficient of the input signal transmitted to the KIPA, $\mathcal{R}$ is reflection coefficient (with $\mathcal{T}^2 + \mathcal{R}^2 = 1$) and $R(\phi)$ is the standard rotation matrix that accounts for a phase shift of ϕ. Figure 16(b) illustrates the effect of a 5% reflection on the measurement of the output of a DPA. In the worst case of $\phi = 0$, the output of the KIPA and the reflected signal constructively interfere and degrade the observed deamplification by approximately 9 dB. The error introduced by the reflected signal will depend on the phase relationship between the KIPA output and the reflected signal, which in general is unknown. To proceed with the analysis, we define an in-phase reflection coefficient $\mathcal{R}'$ and set $\phi = 0$. The in-phase reflection coefficient $\mathcal{R}'$ therefore represents a lower bound for the reflections in the setup needed to explain a given reduction in the observed deamplification level [see Fig. 3(c)].

Using Eq. (G11) combined with the DPA parameters extracted from the fits in Appendix E (κ, $|\xi|$, Δ, etc.), we are able to predict the transformation of a unit magnitude input by the KIPA for different levels of in-phase reflection. We fit the in-phase reflection coefficient to be approximately 2% and find excellent agreement between theory and experiment (see Fig. 17).

The most likely sources of reflections from our setup are the connection from the coaxial lines to our bespoke PCB, and at the wire bonds between the PCB and the chip. Assuming 50-Ω lines down to the sample, a 2% reflection corresponds to an equivalent PCB impedance of

$$Z_{\text{PCB}} = Z_{\text{CPW}} \frac{1 - \mathcal{R}}{1 + \mathcal{R}} = 48\ \Omega, \quad \text{(G12)}$$

which is realistic, accounting for the uncertainty in the design and manufacturing tolerances of the PCB and the temperature dependence of the materials.

The maximum deamplification level G_S is defined as the greatest reduction in amplitude of a coherent input by the phasor transformation, while G_A is the corresponding increase in gain that occurs orthogonal to the axis of deamplification. G_S and G_A are extracted from the ellipse data of Fig. 3(b) and plot in Fig. 3(c). We reproduce the ellipse measurement data here in Fig. 17, along with a set of ellipses generated using our theoretical model. We observe some asymmetry $G_S \neq G_A$ in the data, which is captured accurately by our model that includes weak reflections in the experimental setup [solid lines in Fig. 3(c)]. The ideal amplifier symmetrically transforms both quadratures (i.e., $G_S = G_A$) [5]; however, according to our model for the squeezing transform, symmetry can also be broken if either $Q_i < \infty$ or $|\Delta| > 0$. While some asymmetry is expected, for our estimate of $Q_i = 10^5$, this asymmetry is small, as is evident in Fig. 3(c) (dashed line) where we show the predicted G_S for the reflectionless DPA measurement.

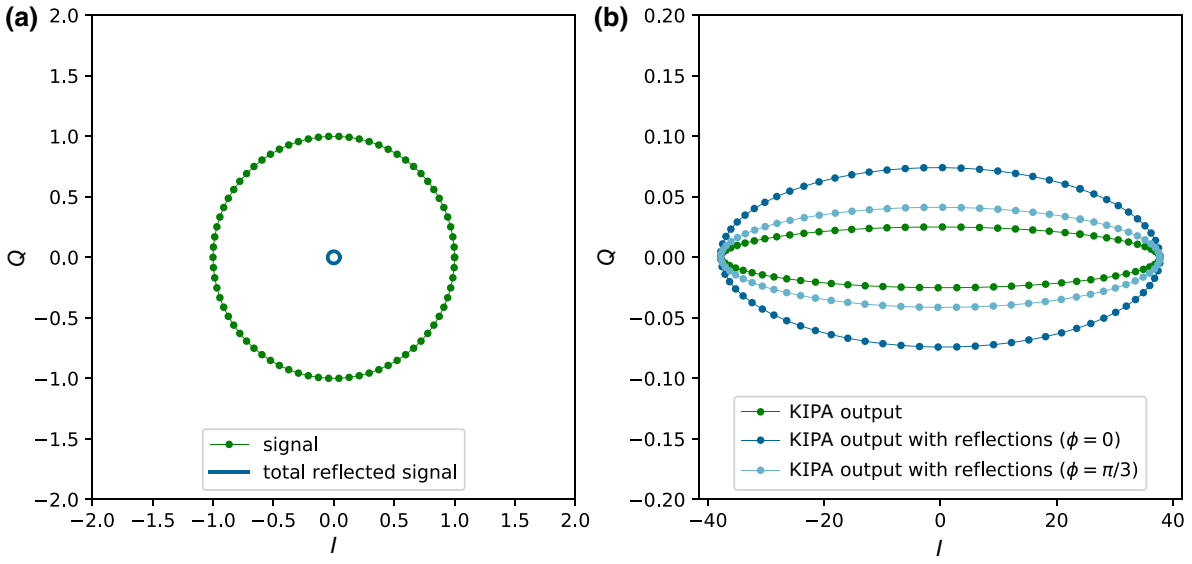

FIG. 16. (a) An input signal (green) represented by points of constant amplitude on the I-Q plane, with a 5% reflected signal (blue). (b) The theoretical output of the KIPA (green) superimposed with the total reflected signal with a phase shift of zero (dark blue) and a phase shift of $\pi/3$ (light blue).

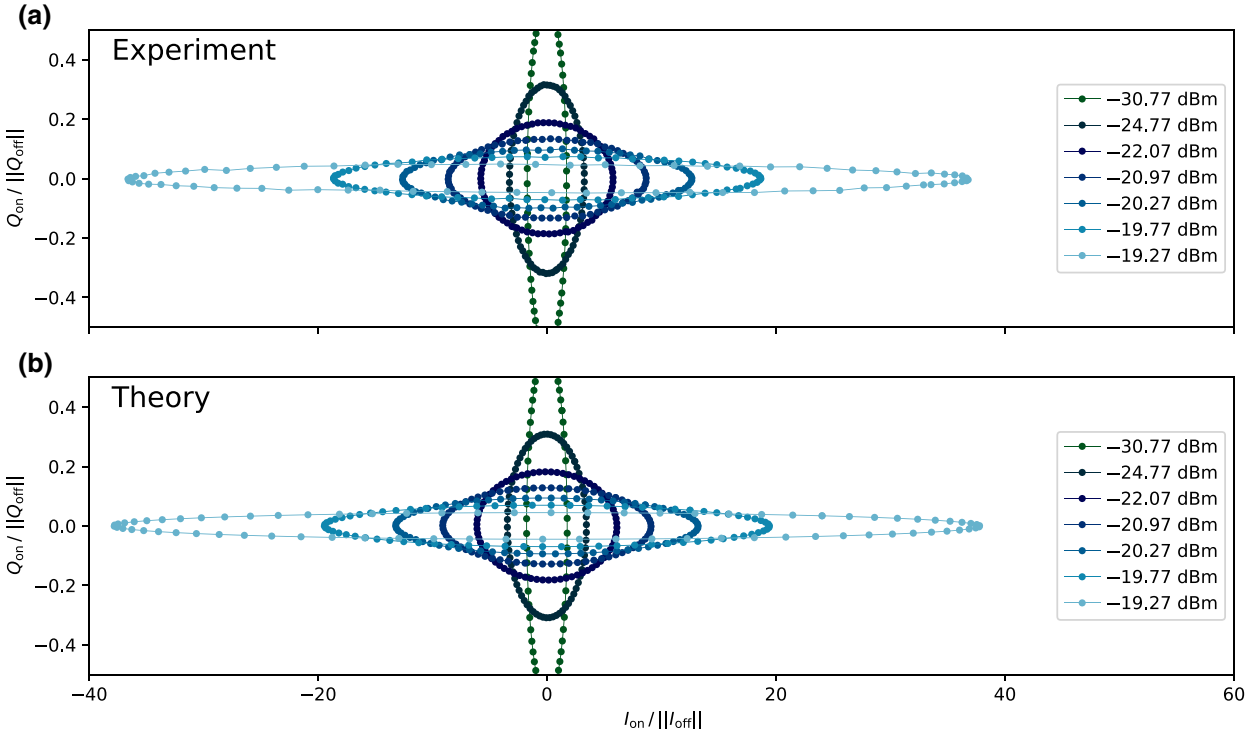

FIG. 17. (a) Ellipses measured by sweeping the phase of a fixed amplitude input, normalized by the amplitude of the input ($||I_{\rm off}||$ or $||Q_{\rm off}||$). These are the same data as presented in Fig. 3(b). Pump powers are shown in the legend. (b) Predicted ellipses from the DPA phasor transformation with a 2% in-phase reflection coefficient.

APPENDIX H: NOISE-SQUEEZING THEORY

In Appendix G we analyzed the gain of the KIPA in phase-sensitive mode when coherent states were applied to its input. In this section we consider the case of a vacuum input state (i.e., noise) and derive expressions for the squeezing (noise deamplification) and antisqueezing (noise amplification) properties of the KIPA. We assume that noise squeezing is measured over a narrow band such that the frequency dependence of g_s and g_i may be ignored, allowing us to draw on the theory presented in Appendix G. In terms of the matrix elements g_{ij} of the phasor transformation matrix A_G, Eq. (G7) becomes

$$\begin{aligned}\begin{pmatrix} I_{\rm out} \\ Q_{\rm out}\end{pmatrix} &= A_G(\theta)\begin{pmatrix} I_{\rm in} \\ Q_{\rm in}\end{pmatrix} \\ &\quad + \sqrt{\frac{\gamma}{\kappa}}\left[A_G(\theta)+1\right]\begin{pmatrix} I_b \\ Q_b\end{pmatrix} \\ &= \begin{pmatrix} g_{11} & g_{12} \\ g_{21} & g_{22}\end{pmatrix}\begin{pmatrix} I_{in} \\ Q_{in}\end{pmatrix} \\ &\quad + \sqrt{\frac{\gamma}{\kappa}}\begin{pmatrix} g_{11}+1 & g_{12} \\ g_{21} & g_{22}+1\end{pmatrix}\begin{pmatrix} I_b \\ Q_b\end{pmatrix}. \end{aligned} \tag{H1}$$

To obtain expressions for the vacuum squeezing, we model the input field as a vacuum state with variances $\langle \Delta I^2\rangle = \langle \Delta Q^2\rangle$ and zero mean: $\langle I\rangle = \langle Q\rangle = 0$. Assuming the bath and the input fields are uncorrelated, and using the fact that $\langle IQ\rangle + \langle QI\rangle = 0$, we may write a system of linear equations for the second-order moments of the output quadratures:

$$\begin{aligned}\begin{pmatrix} \langle I^2_{\rm out}\rangle \\ \langle Q^2_{\rm out}\rangle\end{pmatrix} &= \begin{pmatrix} g^2_{11} & g^2_{12} \\ g^2_{21} & g^2_{22}\end{pmatrix}\begin{pmatrix} \langle I^2_{\rm in}\rangle \\ \langle Q^2_{\rm in}\rangle\end{pmatrix} \\ &\quad + \frac{\gamma}{\kappa}\begin{pmatrix} (g_{11}+1)^2 & g^2_{12} \\ g^2_{21} & (g_{22}+1)^2\end{pmatrix}\begin{pmatrix} \langle I^2_b\rangle \\ \langle Q^2_b\rangle\end{pmatrix}. \end{aligned} \tag{H2}$$

Since the vacuum and bath fields are at the same temperature, we define $\langle \Delta I^2_v\rangle = \langle I^2_{\rm in}\rangle = \langle I^2_b\rangle = 1/4$ and $\langle \Delta Q^2_v\rangle = \langle Q^2_{\rm in}\rangle = \langle Q^2_b\rangle = 1/4$. Thus, the variances of the output quadratures are given by

$$\begin{aligned}\begin{pmatrix} \langle \Delta I^2_{\rm out}\rangle \\ \langle \Delta Q^2_{\rm out}\rangle\end{pmatrix} &= \left[\begin{pmatrix} g^2_{11} & g^2_{12} \\ g^2_{21} & g^2_{22}\end{pmatrix} + \frac{\gamma}{\kappa}\right. \\ &\quad \left.\times \begin{pmatrix} (g_{11}+1)^2 & g^2_{12} \\ g^2_{21} & (g_{22}+1)^2\end{pmatrix}\right]\begin{pmatrix} \langle \Delta I^2_v\rangle \\ \langle \Delta Q^2_v\rangle\end{pmatrix}. \end{aligned} \tag{H3}$$

The increase-decrease in quadrature variance as a function of the pump phase φ_p is described by

$$\mathcal{S}(\varphi_p) = 10\ \log_{10}\frac{\langle \Delta I_{\text{out}}^2 \rangle}{\langle \Delta I_v^2 \rangle} = 10\ \log_{10}\left(g_{11}^2 + g_{12}^2 + \frac{\gamma}{\kappa}[(g_{11}+1)^2 + g_{12}^2]\right), \tag{H4}$$

and the vacuum squeezing level $\mathcal{S}_v$ is defined by the minimum of $\mathcal{S}$,

$$\mathcal{S}_v = \min_{\varphi_p} \mathcal{S}(\varphi_p). \tag{H5}$$

Using the DPA parameters extracted from the phase-insensitive gain features (see Appendix E), we can simulate the expected noise variance gain [Eq. (H4)] as a function of the pump phase. The results are depicted in Fig. 18(a), where we observe a similar phase-dependent response to that measured in Appendix F for strong coherent inputs. In contrast to the phase-sensitive gain for coherent inputs, the coupling of the bath mode into the cavity requires a strictly asymmetric noise variance gain such that $\min_{\varphi_p} S(\varphi_p) \times \max_{\varphi_p} S(\varphi_p) \geq 1$, where equality holds only in the limit of $Q_i \to \infty$. We observe a weak shift in the pump phase corresponding to the point of maximum squeezing as the pump power increases, which is a consequence of the nonzero detuning between the cavity and the pump Δ.

Equipped with this squeezing model and a realistic set of resonator parameters, we can study the effect of Q_i on the maximum attainable squeezing. Figure 18(b) plots the vacuum squeezing level $\mathcal{S}_v$ against the maximum variance gain or antisqueezing gain. In the limit of no losses, Cave's theory predicts symmetric squeezing and antisqueezing with zero-noise photons contributed by the amplifier [5]. We observe here that the squeezing and antisqueezing relationship of the KIPA closely follows the expected symmetric behavior before the squeezing level plateaus to a constant level as the antisqueezing gain increases. The squeezing level plateaus as the total cavity fluctuations are limited by the bath mode variance, which is not squeezed by the KIPA since

$$\begin{pmatrix} A_G + 1 \end{pmatrix} \begin{pmatrix} \text{Var}(I_b) \\ \text{Var}(Q_b) \end{pmatrix} \geq \begin{pmatrix} \text{Var}(I_b) \\ \text{Var}(Q_b) \end{pmatrix}. \tag{H6}$$

We observe an approximately 10-dB improvement in the maximum achievable squeezing for each order-of- magnitude increase in Q_i. The order-of-magnitude improvement in squeezing performance is a result of the corresponding order-of-magnitude decrease in γ/κ, which sets the magnitude of the bath variance contribution to the KIPA output [see Eq. (G7)]. For a $Q_i = 10^5$, our theory predicts up to $\mathcal{S}_v \approx -29$ dB of squeezing could be produced by the KIPA, corresponding to approximately 40 dB of phase-sensitive gain.

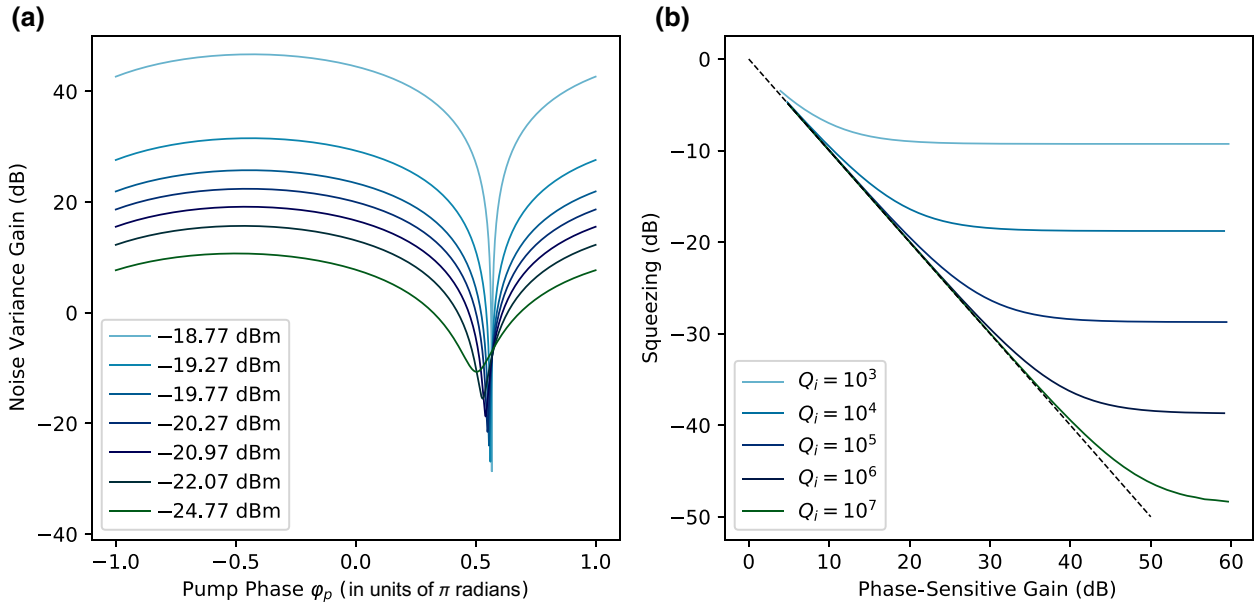

FIG. 18. (a) The simulated noise variance gain $\mathcal{S}(\varphi_p)$ as a function of the pump phase using the DPA parameters obtained in Appendix E, for a range of pump powers. We fix the internal quality factor to $Q_i = 10^5$ in this calculation. (b) The vacuum squeezing level $\mathcal{S}_v$, as a function of the phase-sensitive gain using the DPA parameters obtained in Appendix E for different internal quality factors Q_i. The line of symmetric phase-sensitive gain is plotted (black dashed line).

APPENDIX I: NOISE TEMPERATURE

1. Nondegenerate noise temperature theory

The output fluctuations of the KIPA operating as a nondegenerate amplifier are found from Eq. (D11) to be

$$\begin{aligned}\langle \Delta I_{\text{out}}^2 \rangle &= \left\langle \left[\frac{1}{2}\left(a_{\text{out}}^\dagger + a_{\text{out}} \right) \right]^2 \right\rangle \\ &= \left(|g_s|^2 + \frac{\gamma}{\kappa}|g_s+1|^2 \right)\left(\frac{n_{\text{th}}}{2} + \frac{1}{4} \right) \\ &\quad + |g_i|^2 \left(1 + \frac{\gamma}{\kappa} \right)\left(\frac{n_{\text{th}}}{2} + \frac{1}{4} \right), \end{aligned} \tag{I1}$$

where the signal and idler gains [$g_s(\omega)$ and $g_i(\omega)$] depend on the frequency of the signal being amplified. Here we assume that the input and bath fields (both signal and idler modes) have a thermal occupation $\langle a_{\text{in}}^\dagger a_{\text{in}} \rangle = \langle b_{\text{in}}^\dagger b_{\text{in}} \rangle = n_{\text{th}}$.

One useful identity of the DPA is the relationship between the signal and idler gains [14],

$$|g_i|^2 \left(1 + \frac{\gamma}{\kappa} \right) = |g_s|^2 + \frac{\gamma}{\kappa}|g_s+1|^2 - 1, \tag{I2}$$

which holds for all ω [see Eq. (D12)], and is a by-product of the KIPA output field satisfying the commutation relation $[a_{\text{out}}, a_{\text{out}}^\dagger] = 1$. Substituting Eq. (I2) into our expression for the quadrature fluctuations along I, we obtain

$$\langle \Delta I_{\text{out}}^2 \rangle = \left(|g_s|^2 + \frac{\gamma}{\kappa}|g_s+1|^2 \right)\left(n_{\text{th}} + \frac{1}{2} \right) - \frac{n_{\text{th}}}{2} - \frac{1}{4} \tag{I3}$$

Referring the quadrature fluctuations to the input of the KIPA and subtracting the vacuum contribution, we find:

$$\begin{aligned}\frac{\langle \Delta I_{\text{out}}^2 \rangle}{|g_s|^2} - \frac{1}{4} &= \left(1 + \frac{\gamma}{\kappa}\frac{|g_s+1|^2}{|g_s|^2} \right)\left(n_{\text{th}} + \frac{1}{2} \right) \\ &\quad - \frac{n_{\text{th}}}{2|g_s|^2} - \frac{1}{4|g_s|^2} - \frac{1}{4} \\ &\geq \frac{1}{4}\left(1 - \frac{1}{|g_s|^2} \right) + \frac{\gamma}{\kappa}\frac{|g_s+1|^2}{2|g_s|^2} \\ &\geq \frac{1}{4}\left(1 - \frac{1}{|g_s|^2} \right), \end{aligned} \tag{I4}$$

where in the third line we assume zero temperature ($n_{\text{th}} = 0$) and in the last line we assume no loss ($\gamma = 0$). As required by Cave's fundamental theorem of phase-sensitive amplifiers, the DPA adds 1/4 photons to the input-referred noise in the limit of high gain [5]. Equality only holds in the limit of zero temperature and no losses.

To maintain consistency with the input-output models for phase-sensitive amplifiers used later in this section [e.g., see Eq. (I14)], we write the phase-insensitive output of the KIPA as

$$\langle \Delta I_{\text{out}}^2 \rangle = G_k \left(\frac{n_{\text{th}}}{2} + \frac{1}{4} \right) + (G_k - 1)\left(\frac{n_{\text{th}}}{2} + \frac{n_{\text{kn}}}{2} + \frac{1}{4} \right), \tag{I5}$$

where $G_k = |g_s|^2$ and n_{kn} is the input-referred noise contribution of the KIPA in nondegenerate mode. Comparing Eq. (I3) with the $(G_k - 1)$ term from this expression, we obtain a relation for the additional noise photons contributed by the KIPA n_{kn}:

$$\begin{aligned} n_{\text{kn}} &= \frac{2}{|g_s|^2 - 1}\left[\langle \Delta I_{\text{out}}^2 \rangle - |g_s|^2 \left(\frac{n_{\text{th}}}{2} + \frac{1}{4} \right) \right] \\ &\quad - n_{\text{th}} - \frac{1}{2} \\ &= \frac{2}{|g_s|^2 - 1}\left[\left(\frac{n_{\text{th}}}{2} + \frac{1}{4} \right)(|g_s|^2 - 1) \right. \\ &\quad \left. + \frac{\gamma}{\kappa}|g_s+1|^2 \left(n_{\text{th}} + \frac{1}{2} \right) \right] - n_{\text{th}} - \frac{1}{2} \\ &= \frac{\gamma}{\kappa}\frac{|g_s+1|^2}{|g_s|^2 - 1}(2n_{\text{th}} + 1). \end{aligned} \tag{I6}$$

The temperature dependence for n_{kn} is depicted in Fig. 19 for various ratios of the external and internal quality factors Q_c/Q_i, and using the same DPA parameters as were measured previously. Compared to n_{th}, the change in n_{kn} is small across the range of internal quality factors considered. At zero temperature n_{kn} appears to decrease by an approximate order of magnitude for every decrease in the order of magnitude of $Q_c/Q_i = \gamma/\kappa$, further motivating the desire to maximize the Q_i of a DPA.

We define the zero temperature noise as

$$n_{\text{kn0}} = \frac{\gamma}{\kappa}\frac{|g_s+1|^2}{|g_s|^2 - 1}, \tag{I7}$$

and plot n_{kn0} as a function of Q_c/Q_i in Fig. 19(c), where we observe rapid convergence to zero as $Q_c/Q_i \to 0$.

2. Degenerate noise temperature theory

The output fluctuations of the KIPA in degenerate mode as a function of the pump phase φ_p are given by (see Appendix H)

$$\begin{aligned}\langle \Delta I_{\text{out}}(\varphi_p)^2 \rangle &= |g_s + g_i^*(\varphi_p)|^2 \left(\frac{n_{\text{th}}}{2} + \frac{1}{4} \right) \\ &\quad + \frac{\gamma}{\kappa}|g_s + 1 + g_i^*(\varphi_p)|^2 \left(\frac{n_{\text{th}}}{2} + \frac{1}{4} \right), \end{aligned} \tag{I8}$$

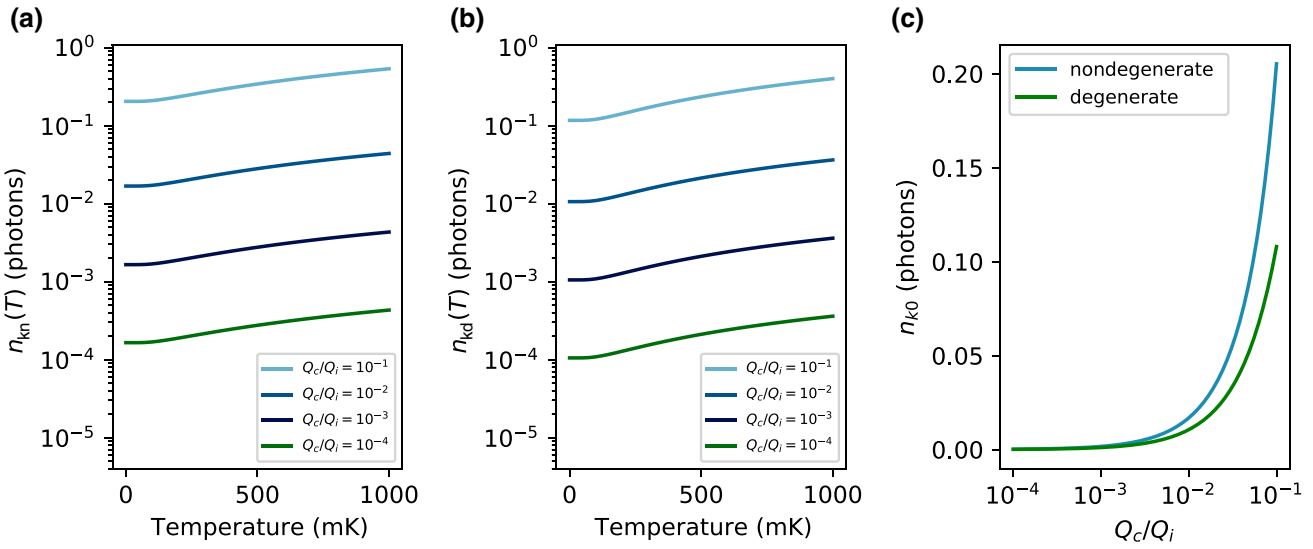

FIG. 19. (a) The simulated nondegenerate noise photon number $n_{\rm kn}$ as a function of temperature for different values of Q_c/Q_i. (b) The simulated degenerate noise photon number $n_{\rm kd}$ as a function of temperature for different values of Q_c/Q_i. (c) The simulated nondegenerate (degenerate) noise photon number at zero temperature as a function of Q_c/Q_i. All calculations performed at a nondegenerate (degenerate) gain of $G_k = 25$ dB (31 dB).

with phase-sensitive power gain $G_k(\varphi_p) = |g_s + g_i^*(\varphi_p)|^2$. Referred to the KIPA input, the excess quadrature fluctuations contributed by the amplifier are

$$\frac{\langle \Delta I_{\rm out}(\varphi_p)^2\rangle}{G_k(\varphi_p)} - \frac{1}{4} = \frac{n_{\rm th}}{2} + \frac{\gamma}{\kappa}\frac{|g_s + 1 + g_i^*(\varphi_p)|^2}{|g_s + g_i^*(\varphi_p)|^2} \times \left(\frac{n_{\rm th}}{2} + \frac{1}{4}\right) \geq 0. \tag{I9}$$

As predicted by Caves, the excess quadrature fluctuations referred to the input can be as small as zero in limit of $\hbar\omega \ll k_B T$ and provided there are no losses in the system (i.e., $\gamma = 0$) [5].

Writing $G_k = |g_s + g_i^*(\varphi_p)|^2$, we define a similar expression to Eq. (I5) for the phase-sensitive amplifier along the amplified quadrature:

$$\langle \Delta I_{\rm out}^2\rangle = G_k\left(\frac{n_{\rm th}}{2} + \frac{1}{4}\right) + (G_k - 1)\left(\frac{n_{\rm kd}}{2}\right), \tag{I10}$$

with

$$n_{\rm kd} = \frac{\gamma}{\kappa}\frac{|g_s + 1 + g_i^*|^2}{|g_s + g_i^*|^2 - 1}\left(n_{\rm th} + \frac{1}{2}\right) \tag{I11}$$

$$n_{\rm kd0} = \frac{\gamma}{2\kappa}\frac{|g_s + 1 + g_i^*|^2}{|g_s + g_i^*|^2 - 1}. \tag{I12}$$

Again, we simulate $n_{\rm kd}$ for varied ratios $Q_c/Q_i = \gamma/\kappa$ and temperatures and find similar behavior to the nondegenerate case.

3. Noise temperature measurement

The detection chain of the KIPA consists of a series of amplifiers and attenuators, which we depict in Fig. 20(a). Directly after the KIPA there are microwave losses associated with the diplexer, the circulator, and the microwave lines. To model the detection chain we divide these losses into two effective attenuators, one at 20 mK and the other at 4 K. Each attenuator acts like an optical beam splitter, where the transmitted field is reduced by $\sqrt{\alpha}$ and the open port mixes the thermal field v into the output according to the beam splitter equation [67]

$$a_{\rm out} = \sqrt{\alpha}a_{\rm in} + \sqrt{1-\alpha}v. \tag{I13}$$

At 4 K we have the HEMT amplifier, followed by a second microwave amplifier at room temperature. Each amplifier contributes additional noise to its output field [5]:

$$a_{\rm out} = \sqrt{G_{\rm amp}}a_{\rm in} + \sqrt{G_{\rm amp} - 1}h^\dagger. \tag{I14}$$

Combining the attenuator models for α_1 and α_2 [Eq. (I13)] with the amplifier models for the HEMT and room-temperature amplifier [Eq. (I14)], we may simplify the detection chain to a single equivalent amplifier with gain G_T and noise contribution $h_{\rm tot}$ [see Fig. 20(b)]. The total output field at the end of the detection chain is given by

$$a_{\rm tot} = \sqrt{G_T}a_{\rm out} + \sqrt{G_T - 1}h_{\rm tot}^\dagger, \tag{I15}$$

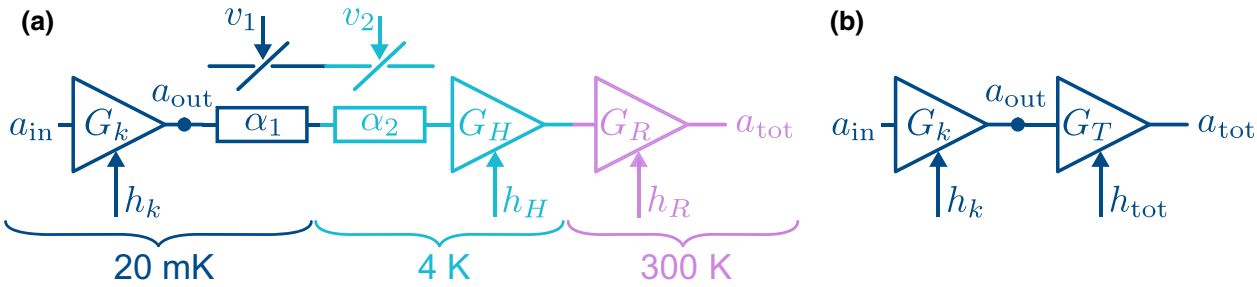

FIG. 20. (a) The complete detection chain model, consisting of the KIPA and attenuator α_1 at 20 mK, attenuator α_2, and the HEMT at 4 K, and the room-temperature amplifier at 300 K. The attenuators are modeled as beam splitters, mixing in the thermal operators v_1 and v_2 with the detected field as it propagates along the detection chain. Each amplifier contributes noise to its output, denoted here by the field operators h_k (KIPA), h_H (HEMT), and h_R (room-temperature amplifier). (b) The simplified detection chain model, where the attenuators and amplifiers after the KIPA may be modeled as an effective amplifier with gain G_T and noise field h_{tot}.

where,

$$G_T = G_R G_H \alpha_1 \alpha_2,$$

$$h_{\text{tot}}^\dagger = \sqrt{\frac{G_R G_H}{G_T - 1}}\left[\sqrt{\alpha_1(1-\alpha_1)}v_1 + \sqrt{(1-\alpha_2)}v_2 + \sqrt{\frac{G_H - 1}{G_H}}h_H^\dagger + \sqrt{\frac{G_R - 1}{G_R G_H}}h_R^\dagger\right].$$

Rewriting the output field a_{out} as a pump-phase-dependent quadrature operator $I_{\text{out}}(\varphi_p) = (a_{\text{out}}^\dagger e^{-i\varphi_p} + a_{\text{out}} e^{i\varphi_p})/2$, we have

$$I_{\text{tot}}(\varphi_p) = \sqrt{G_T} I_{\text{out}}(\varphi_p) + \sqrt{G_T - 1} I_h(-\varphi_p), \tag{I16}$$

where $I_{\text{out}}(\varphi_p)$ is the pump-phase-dependent quadrature operator at the KIPA output, and I_h is the detection chain noise quadrature operator $I_h(-\varphi_p) = (h_{\text{tot}}^\dagger e^{i\varphi_p} + h_{\text{tot}} e^{-i\varphi_p})/2$.

Assuming h_{tot} and a_{out} are composed of uncorrelated thermal states, the quadrature fluctuations at the detector simplify to

$$\begin{aligned}\langle \Delta I_{\text{tot}}^2 \rangle &= G_T \langle \Delta I_{\text{out}}^2 \rangle + (G_T - 1)\langle \Delta I_h^2 \rangle \\ &= G_T \langle \Delta I_{\text{out}}^2 \rangle + (G_T - 1)\left(\frac{n_{\text{sys}}}{2} + \frac{1}{4}\right),\end{aligned} \tag{I17}$$

where we introduce the effective system noise photon number n_{sys}, given by

$$\begin{aligned}n_{\text{sys}} &= \langle h_{\text{tot}}^\dagger h_{\text{tot}} \rangle \\ &= \frac{G_R G_H}{G_T - 1}\left[\alpha_2(1-\alpha_1)(n_{20\text{mK}} + 1) + (1-\alpha_2)(n_{4\text{K}} + 1) + \frac{G_H - 1}{G_H} n_H + \frac{G_R - 1}{G_R G_H} n_R\right],\end{aligned} \tag{I18}$$

which is the number of noise photons added by the system (due to loss and the following amplifiers) referred to the output of the KIPA.

The average microwave noise power that would be measured by a spectrum analyzer is simply the sum of the output quadrature variances:

$$P_{\text{tot}} = z(\langle \Delta I_{\text{tot}}^2 \rangle + \langle \Delta Q_{\text{tot}}^2 \rangle). \tag{I19}$$

We introduce the parameter z here that converts the units from photons to watts as is measured by the spectrum analyzer over a certain measurement bandwidth resolution.

In nondegenerate operation, the variance of both the KIPA output and the system noise fields is independent of the pump phase, allowing us to write the measured microwave power as

$$\begin{aligned}P_{\text{tn}} &= z G_T(\langle \Delta I_{\text{out}}^2 \rangle + \langle \Delta Q_{\text{out}}^2 \rangle) + z(G_T - 1)\left(n_{\text{sys}} + \frac{1}{2}\right) \\ &= 2 z G_T \langle \Delta I_{\text{out}}^2 \rangle + z(G_T - 1)\left(n_{\text{sys}} + \frac{1}{2}\right).\end{aligned} \tag{I20}$$

In nondegenerate mode, the output fluctuations of the KIPA are given by (see Sec. I 1)

$$\langle \Delta I_{\text{out}}^2 \rangle = G_k\left(\frac{n_{\text{th}}}{2} + \frac{1}{4}\right) + (G_k - 1)\left(\frac{n_{\text{th}}}{2} + \frac{n_{\text{kn}}}{2} + \frac{1}{4}\right), \tag{I21}$$

with $G_k = |g_s|^2$ as defined in Eq. (D12), thermal noise population $n_{\text{th}} = \langle a_{\text{in}}^\dagger a_{\text{in}} \rangle$, and an additional number of noise photons added by the KIPA, $n_{\text{kn}} = \langle h_k^\dagger h_k \rangle$. In the nondegenerate case, the idler mode contributes a minimum $n_{\text{th}}/2 + 1/4$ input-referred photons to the variance of each quadrature at the signal frequency, while an additional $n_{\text{kn}}/2$ photons arise from internal cavity losses. We note that it is important to include the effect of the idler to correctly capture the temperature dependence of the output noise, as discussed in recent work on traveling-wave

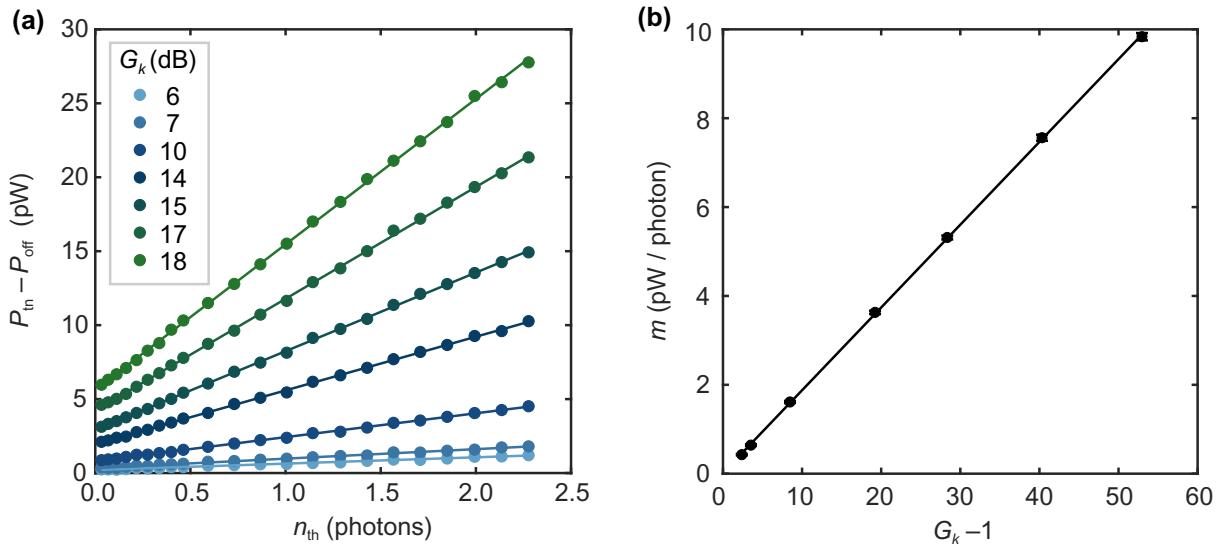

FIG. 21. (a) The difference power reported by the spectrum analyzer for the KIPA on vs off in nondegenerate mode as a function of the thermal photon population at the mixing plate for different nondegenerate gains (see legend). Solid lines are linear fits. (b) The gradient m of the linear fits presented in (a) ($P_{tn} - P_{off} = m \times n_{th} + b$) versus $G_k - 1 = |g_s|^2 - 1$.

devices [27,68]. The excess noise n_{kn} is expected to vary with temperature (see Appendix I 1); however, for $Q_i > 10^4$ (or $Q_c/Q_i < 10^{-2}$) this dependence is predicted to be weak.

Substituting Eq. (I21) into Eq. (I20), we arrive at

$$P_{tn} = zG_TG_k\left(n_{th} + \frac{1}{2}\right) + zG_T(G_k - 1)\left(n_{th} + n_{kn} + \frac{1}{2}\right) + z(G_T - 1)\left(n_{sys} + \frac{1}{2}\right). \quad \text{(I22)}$$

It is instructive to restate the origin of each component in Eq. (I22). The first term, $zG_TG_k(n_{th} + 1/2)$, represents the noise at the output due to the signal, while the second term, $zG_T(G_k - 1)(n_{th} + n_{kn} + 1/2)$, is the output noise contributed by the idler [$zG_T(G_k - 1)(n_{th} + 1/2)$] together with the excess KIPA noise that mixes in through the internal amplifier loss [$zG_T(G_k - 1)n_{kn}$]. The final term, $z(G_T - 1)(n_{sys} + 1/2)$, represents the total noise added by components in the chain after the KIPA.

Both n_{sys} and the conversion factor zG_T in Eq. (I22) are unknown. We begin by finding zG_T, observing that when the KIPA is off (i.e., $G_k = 1$), Eq. (I22) simplifies to

$$P_{off} = zG_T\left(n_{th} + \frac{1}{2}\right) + z(G_T - 1)\left(n_{sys} + \frac{1}{2}\right). \quad \text{(I23)}$$

Evaluating the difference in power between when the KIPA is on compared to off removes the dependence on n_{sys}:

$$P_{tn} - P_{off} = zG_T(G_k - 1)\left(2n_{th} + n_{kn} + 1\right). \quad \text{(I24)}$$

To extract zG_T we sweep the temperature of the mixing chamber of our dilution refrigerator (and thus n_{th}) while operating the KIPA as a nondegenerate amplifier (500-kHz detuned from $\omega_p/2$). At each temperature, we measure the noise power at the output of our detection chain using a spectrum analyzer configured in zero-span mode with a measurement bandwidth of 130 kHz. We constrain the experiment to nondegenerate gains below 20 dB,

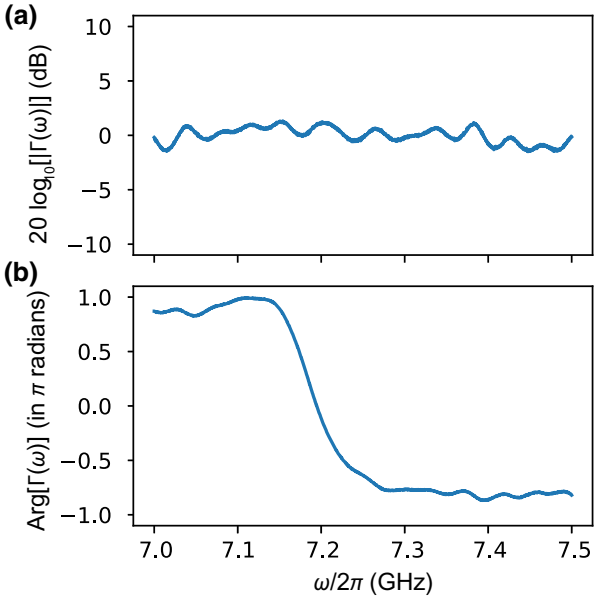

FIG. 22. (a) Measured magnitude and (b) phase response of the KIPA investigated in this work. No pump is applied in this measurement and $I_{dc} = 0.85$ mA.

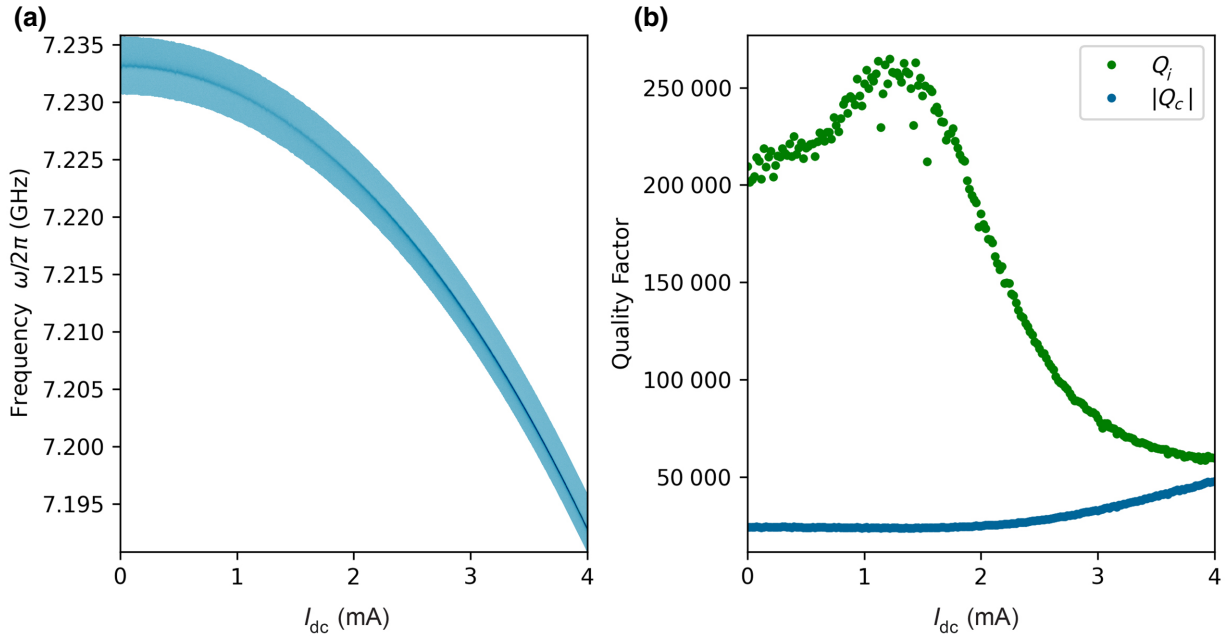

FIG. 23. (a) Measured magnitude response of a similar device to the KIPA, as a function of I_{dc}. (b) Coupling and internal quality factors extracted from fits to the magnitude response in panel (a).

since below this the KIPA gain responses are completely flat over the 500 kHz detuned measurement band and we can therefore approximate G_k by measuring the gain using a (narrow band) coherent tone. At each KIPA gain $G_k = |g_s|^2$ we expect the difference in power to increase linearly according to $P_{tn} - P_{off} = m \times n_{th} + b$ with gradient $m = 2zG_T(G_k - 1)$. The data are shown in Fig. 21(a), which displays a clear linearity with n_{th} for various nondegenerate gains. We plot m against $G_k - 1$ and extract the conversion factor $zG_T = 93.2$ fW/photon [see Fig. 21(b)]. This analysis relies on the assumptions that zG_T is independent of both gain and temperature. These assumptions are not verified here and may lead to an overestimation of zG_T, since, for example, n_{kn} in Eq. (I24) might exhibit slight G_k and n_{th} dependencies in practice. We therefore caution that the extracted conversion factor allows for an estimation of the noise performance only; a more rigorous measurement using a calibrated cryogenic noise source should permit a precise evaluation of the KIPA noise in the future.

The conversion factor zG_T includes the total gain and attenuation from the output of the KIPA to the spectrum analyzer (i.e., $G_T = \alpha_1\alpha_2 G_H G_R$). It therefore allows us to calculate an equivalent number of noise photons referred to the KIPA output plane from a measurement of the noise power at the output of the detection chain. Combining this with the KIPA gain G_k (i.e., zG_TG_k), we can refer the noise to the input plane of the KIPA.

We can provide an estimate of the system noise n_{sys} (which is referred to the output of the KIPA) using Eq. (I23):

$$n_{sys} \approx \frac{P_{off}}{zG_T} - (n_{th} + 1). \tag{I25}$$

Taking the noise power measured with the KIPA off at base temperature (where $\hbar\omega \ll k_BT$) and thus assuming $n_{th} \ll 1$, we calculate $n_{sys} = 81.5$ photons. To validate our estimate of n_{sys}, we substitute data-sheet values for the HEMT and room-temperature amplifier into Eq. (I18) and estimate α_1 and α_2 based on manufacturer values for cable, circulator, and diplexer insertion losses. Equation (I18) then gives $n_{sys} \approx 64$ photons. This discrepancy could be explained by a 1-dB uncertainty in the estimate of the losses, which we believe represents a reasonable agreement.

Finally, we turn our attention now to the degenerate gain. Because the fluctuations along one quadrature of the KIPA output are squeezed and are therefore considerably smaller than the fluctuations along the orthogonal amplified quadrature, the total noise power measured at the spectrum analyzer may be approximated by

$$\begin{aligned} P_{td} &= zG_T(\langle\Delta I_{out}^2\rangle + \langle\Delta Q_{out}^2\rangle) + z(G_T - 1)\left(n_{sys} + \frac{1}{2}\right) \\ &\approx zG_T\langle\Delta I_{out}^2\rangle + z(G_T - 1)\left(n_{sys} + \frac{1}{2}\right). \end{aligned} \tag{I26}$$

From Eq. (I10), we have

$$P_{\rm td} = zG_TG_k\left(\frac{n_{\rm th}}{2}+\frac{1}{4}\right)+zG_T(G_k-1)\left(\frac{n_{\rm kd}}{2}\right) + z(G_T-1)\left(n_{\rm sys}+\frac{1}{2}\right). \quad \text{(I27)}$$

The first term in Eq. (I27), $zG_TG_k(n_{\rm th}/2+1/4)$, originates from noise in the input field, which is amplified along a single quadrature in degenerate mode. The second term, $zG_T(G_k-1)n_{\rm kd}/2$, comes from the noise that mixes in through the internal amplifier loss (i.e., the KIPA excess noise). The last term, $z(G_T-1)(n_{\rm sys}+1/2)$, represents the noise added by components in the chain after the KIPA, which is taken for both field quadratures since detection is performed using a spectrum analyzer that measures the total power of the amplified output field.

4. Signal line attenuation

In Fig. 4(b) we plot the input-referred number of photons recorded in the presence of an applied coherent tone, with the KIPA in three different configurations: degenerate mode, nondegenerate mode, and off. We calculate the input-referred number of photons by dividing the measured output power by zG_TG_k and then the equivalent input-referred power by multiplying the number of photons by $\hbar\omega_0 B$, where $B = 1$ kHz is the measurement bandwidth resolution. Knowing the power at the output of the signal generator (-60 dBm) used in this measurement, the input-referred coherent tone power (-132 dBm) can be used to calculate a 72-dB loss along the input signal line. This loss is consistent with the 60 dB of fixed attenuation in our setup, plus our estimates for additional cable and component insertion loss based on manufacturer data sheets.

APPENDIX J: KIPA LOSSES

The KIPA operates in the overcoupled regime, where the external coupling rate far exceeds the rate of internal losses ($\kappa \gg \gamma$). As such, the magnitude response in the absence of a pump tone [Fig. 22(a)] is flat, as predicted by input-output theory [Eq. (E1)]. We can place a lower bound on the internal quality factor based on the ripple of approximately 0.7 dB observed in our reflection measurement, which indicates $Q_i > 3350$.

Figure 23 depicts the reflection response of a device similar to the KIPA, fabricated on a 50-nm-thick $Nb_xTi_{1-x}N$ film and with additional cells in the band-stop region to produce a larger external quality factor (i.e., smaller κ). This device operates close to critical coupling where both $\gamma = \omega_0/Q_i$ and $\kappa = \omega_0/Q_c$ may be extracted. Although resonator losses are sensitive to the exact device geometry, this measurement provides an indication of the attainable internal quality factors for step-impedance filter-coupled microwave resonators.

We note that the loss in the KIPA will almost certainly depend on its operating conditions. Large intracavity fields can induce two-photon losses [23,60] and we observe a nontrivial dependence of Q_i on the dc current bias [Fig. 23(b)]. Future work will explore the noise properties of the KIPA in further detail, including the search for optimal working points in the device parameter space that maximize noise squeezing.

[1] R. Vijay, D. Slichter, and I. Siddiqi, Observation of Quantum Jumps in a Superconducting Artificial Atom, Phys. Rev. Lett. **106**, 110502 (2011).

[2] V. Ranjan, S. Probst, B. Albanese, T. Schenkel, D. Vion, D. Esteve, J. J. L. Morton, and P. Bertet, Electron spin resonance spectroscopy with femtoliter detection volume, Appl. Phys. Lett. **116**, 184002 (2020).

[3] M. Malnou, D. A. Palken, B. M. Brubaker, L. R. Vale, G. C. Hilton, and K. W. Lehnert, Squeezed Vacuum Used to Accelerate the Search for a Weak Classical Signal, Phys. Rev. X **9**, 021023 (2019).

[4] K. Backes, D. Palken, S. Al Kenany, B. Brubaker, S. Cahn, A. Droster, G. C. Hilton, S. Ghosh, H. Jackson, and S. Lamoreaux *et al.*, A quantum enhanced search for dark matter axions, Nature **590**, 238 (2021).

[5] C. M. Caves, Quantum limits on noise in linear amplifiers, Phys. Rev. D **26**, 1817 (1982).

[6] W. F. Kindel, M. D. Schroer, and K. W. Lehnert, Generation and efficient measurement of single photons from fixed-frequency superconducting qubits, Phys. Rev. A **93**, 033817 (2016).

[7] J. Aasi, J. Abadie, B. Abbott, R. Abbott, T. Abbott, M. Abernathy, C. Adams, T. Adams, P. Addesso, and R. Adhikari *et al.*, Enhanced sensitivity of the ligo gravitational wave detector by using squeezed states of light, Nat. Photonics **7**, 613 (2013).

[8] B. Yurke, L. R. Corruccini, P. G. Kaminsky, L. W. Rupp, A. D. Smith, A. H. Silver, R. W. Simon, and E. A. Whittaker, Observation of parametric amplification and deamplification in a josephson parametric amplifier, Phys. Rev. A **39**, 2519 (1989).

[9] A. Roy and M. Devoret, Introduction to parametric amplification of quantum signals with josephson circuits, C. R. Phys. **17**, 740 (2016).

[10] M. A. Castellanos-Beltran, K. D. Irwin, G. C. Hilton, L. R. Vale, and K. W. Lehnert, Amplification and squeezing of quantum noise with a tunable Josephson metamaterial, Nat. Phys. **4**, 929 (2008).

[11] C. Eichler, Y. Salathe, J. Mlynek, S. Schmidt, and A. Wallraff, Quantum-Limited Amplification and Entanglement in Coupled Nonlinear Resonators, Phys. Rev. Lett. **113**, 110502 (2014).

[12] A. Bienfait, P. Campagne-Ibarcq, A. Kiilerich, X. Zhou, S. Probst, J. Pla, T. Schenkel, D. Vion, D. Esteve, J. Morton, and P. Bertet, Magnetic Resonance with Squeezed Microwaves, Phys. Rev. X **7**, 041011 (2017).

[13] M. Malnou, D. Palken, L. R. Vale, G. C. Hilton, and K. Lehnert, Optimal Operation of a Josephson Parametric Amplifier for Vacuum Squeezing, Phys. Rev. Appl. **9**, 044023 (2018).

[14] S. Boutin, D. M. Toyli, A. V. Venkatramani, A. W. Eddins, I. Siddiqi, and A. Blais, Effect of Higher-Order Nonlinearities on Amplification and Squeezing in Josephson Parametric Amplifiers, Phys. Rev. Appl. **8**, 054030 (2017).

[15] X. Zhou, V. Schmitt, P. Bertet, D. Vion, W. Wustmann, V. Shumeiko, and D. Estève, High-gain weakly nonlinear flux-modulated josephson parametric amplifier using a squid array, Phys. Rev. B **89**, 214517 (2014).

[16] L. Planat, R. Dassonneville, J. P. Martínez, F. Foroughi, O. Buisson, W. Hasch-Guichard, C. Naud, R. Vijay, K. Murch, and N. Roch, Understanding the Saturation Power of Josephson Parametric Amplifiers Made from Squid Arrays, Phys. Rev. Appl. **11**, 034014 (2019).

[17] J. Grebel, A. Bienfait, É. Dumur, H.-S. Chang, M.-H. Chou, C. Conner, G. Peairs, R. Povey, Y. Zhong, and A. Cleland, Flux-pumped impedance-engineered broadband josephson parametric amplifier, Appl. Phys. Lett. **118**, 142601 (2021).

[18] N. Frattini, V. Sivak, A. Lingenfelter, S. Shankar, and M. Devoret, Optimizing the Nonlinearity and Dissipation of a Snail Parametric Amplifier for Dynamic Range, Phys. Rev. Appl. **10**, 054020 (2018).

[19] V. Sivak, N. Frattini, V. Joshi, A. Lingenfelter, S. Shankar, and M. Devoret, Kerr-Free Three-Wave Mixing in Superconducting Quantum Circuits, Phys. Rev. Appl. **11**, 054060 (2019).

[20] V. V. Sivak, S. Shankar, G. Liu, J. Aumentado, and M. H. Devoret, Josephson Array-Mode Parametric Amplifier, Phys. Rev. Appl. **13**, 024014 (2020).

[21] T.-C. Chien, O. Lanes, C. Liu, X. Cao, P. Lu, S. Motz, G. Liu, D. Pekker, and M. Hatridge, Multiparametric amplification and qubit measurement with a kerr-free josephson ring modulator, Phys. Rev. A **101**, 042336 (2020).

[22] E. A. Tholén, A. Ergül, K. Stannigel, C. Hutter, and D. B. Haviland, Parametric amplification with weak-link nonlinearity in superconducting microresonators, Physica Scripta **T137**, 014019 (2009).

[23] B. H. Eom, P. K. Day, H. G. LeDuc, and J. Zmuidzinas, A wideband, low-noise superconducting amplifier with high dynamic range, Nat. Phys. **8**, 623 (2012).

[24] M. R. Vissers, R. P. Erickson, H.-S. Ku, L. Vale, X. Wu, G. C. Hilton, and D. P. Pappas, Low-noise kinetic inductance traveling-wave amplifier using three-wave mixing, Appl. Phys. Lett. **108**, 012601 (2016).

[25] S. Chaudhuri, D. Li, K. Irwin, C. Bockstiegel, J. Hubmayr, J. Ullom, M. Vissers, and J. Gao, Broadband parametric amplifiers based on nonlinear kinetic inductance artificial transmission lines, Appl. Phys. Lett. **110**, 152601 (2017).

[26] A. Anferov, A. Suleymanzade, A. Oriani, J. Simon, and D. I. Schuster, Millimeter-Wave Four-Wave Mixing via Kinetic Inductance for Quantum Devices, Phys. Rev. Appl. **13**, 024056 (2020).

[27] M. Malnou, M. Vissers, J. Wheeler, J. Aumentado, J. Hubmayr, J. Ullom, and J. Gao, Three-wave mixing kinetic inductance traveling-wave amplifier with near-quantum-limited noise performance, PRX Quantum **2**, 010302 (2021).

[28] A. J. Annunziata, D. F. Santavicca, L. Frunzio, G. Catelani, M. J. Rooks, A. Frydman, and D. E. Prober, Tunable superconducting nanoinductors, Nanotechnology **21**, 445202 (2010).

[29] J. Zmuidzinas, Superconducting microresonators: Physics and applications, Annu. Rev. Condens. Matter Phys. **3**, 169 (2012).

[30] R. P. Erickson and D. P. Pappas, Theory of multiwave mixing within the superconducting kinetic-inductance traveling-wave amplifier, Phys. Rev. B **95**, 104506 (2017).

[31] N. Samkharadze, A. Bruno, P. Scarlino, G. Zheng, D. P. DiVincenzo, L. DiCarlo, and L. M. K. Vandersypen, High-Kinetic-Inductance Superconducting Nanowire Resonators for Circuit qed in a Magnetic Field, Phys. Rev. Appl. **5**, 044004 (2016).

[32] L. Zhang, W. Peng, L. X. You, and Z. Wang, Superconducting properties and chemical composition of nbtin thin films with different thickness, Appl. Phys. Lett. **107**, 122603 (2015).

[33] A. Bruno, G. de Lange, S. Asaad, K. L. van der Enden, N. K. Langford, and L. DiCarlo, Reducing intrinsic loss in superconducting resonators by surface treatment and deep etching of silicon substrates, Appl. Phys. Lett. **106**, 182601 (2015).

[34] T.-Y. Yun and K. Chang, in *1999 IEEE MTT-S International Microwave Symposium Digest (Cat. No. 99CH36282)*, Vol. 4 (IEEE, 1999), p. 1629.

[35] A. J. Sigillito, A. M. Tyryshkin, T. Schenkel, A. A. Houck, and S. A. Lyon, All-electric control of donor nuclear spin qubits in silicon, Nat. Nanotechnol. **12**, 958 (2017).

[36] E. Zakka-Bajjani, F. Nguyen, M. Lee, L. R. Vale, R. W. Simmonds, and J. Aumentado, Quantum superposition of a single microwave photon in two different' colour' states, Nat. Phys. **7**, 599 (2011).

[37] T. Yamamoto, K. Inomata, M. Watanabe, K. Matsuba, T. Miyazaki, W. D. Oliver, Y. Nakamura, and J. Tsai, Flux-driven josephson parametric amplifier, Appl. Phys. Lett. **93**, 042510 (2008).

[38] C. Eichler and A. Wallraff, Controlling the dynamic range of a josephson parametric amplifier, EPJ Quantum Technol. **1**, 1 (2014).

[39] B. Ho Eom, P. K. Day, H. G. LeDuc, and J. Zmuidzinas, A wideband, low-noise superconducting amplifier with high dynamic range, Nat. Phys. **8**, 623 (2012).

[40] E. Hyyppä, M. Jenei, S. Masuda, V. Sevriuk, K. Tan, M. Silveri, J. Goetz, M. Partanen, R. Lake, and L. Grönberg *et al.*, Calibration of cryogenic amplification chains using normal-metal–insulator–superconductor junctions, Appl. Phys. Lett. **114**, 192603 (2019).

[41] R. Barends, N. Vercruyssen, A. Endo, P. De Visser, T. Zijlstra, T. Klapwijk, P. Diener, S. Yates, and J. Baselmans, Minimal resonator loss for circuit quantum electrodynamics, Appl. Phys. Lett. **97**, 023508 (2010).

[42] N. C. Menicucci, P. van Loock, M. Gu, C. Weedbrook, T. C. Ralph, and M. A. Nielsen, Universal Quantum Computation with Continuous-Variable Cluster States, Phys. Rev. Lett. **97**, 110501 (2006).

[43] W. Asavanant, Y. Shiozawa, S. Yokoyama, B. Charoensombutamon, H. Emura, R. N. Alexander, S. Takeda, J.-i. Yoshikawa, N. C. Menicucci, and H. Yonezawa *et al.*, Generation of time-domain-multiplexed two-dimensional cluster state, Science **366**, 373 (2019).

[44] N. C. Menicucci, Fault-Tolerant Measurement-Based Quantum Computing with Continuous-Variable Cluster States, Phys. Rev. Lett. **112**, 120504 (2014).

[45] M. Hofheinz, E. Weig, M. Ansmann, R. C. Bialczak, E. Lucero, M. Neeley, A. O'connell, H. Wang, J. M. Martinis, and A. Cleland, Generation of fock states in a superconducting quantum circuit, Nature **454**, 310 (2008).

[46] A. L. Grimsmo and A. Blais, Squeezing and quantum state engineering with Josephson travelling wave amplifiers, Npj Quantum Inf. **3**, 1 (2017).

[47] A. Grimm, N. E. Frattini, S. Puri, S. O. Mundhada, S. Touzard, M. Mirrahimi, S. M. Girvin, S. Shankar, and M. H. Devoret, Stabilization and operation of a kerr-cat qubit, Nature **584**, 205 (2020).

[48] A. Mahoney, J. Colless, S. Pauka, J. Hornibrook, J. Watson, G. Gardner, M. Manfra, A. Doherty, and D. Reilly, On-Chip Microwave Quantum Hall Circulator, Phys. Rev. X **7**, 011007 (2017).

[49] B. J. Chapman, E. I. Rosenthal, J. Kerckhoff, B. A. Moores, L. R. Vale, J. Mates, G. C. Hilton, K. Lalumiere, A. Blais, and K. Lehnert, Widely Tunable On-Chip Microwave Circulator for Superconducting Quantum Circuits, Phys. Rev. X **7**, 041043 (2017).

[50] S. Barzanjeh, M. Wulf, M. Peruzzo, M. Kalaee, P. Dieterle, O. Painter, and J. M. Fink, Mechanical on-chip microwave circulator, Nat. Commun. **8**, 1 (2017).

[51] B. J. Chapman, E. I. Rosenthal, and K. Lehnert, Design of an On-Chip Superconducting Microwave Circulator with Octave Bandwidth, Phys. Rev. Appl. **11**, 044048 (2019).

[52] S. Schaal, I. Ahmed, J. Haigh, L. Hutin, B. Bertrand, S. Barraud, M. Vinet, C.-M. Lee, N. Stelmashenko, and J. Robinson *et al.*, Fast Gate-Based Readout of Silicon Quantum Dots Using Josephson Parametric Amplification, Phys. Rev. Lett. **124**, 067701 (2020).

[53] A. West, B. Hensen, A. Jouan, T. Tanttu, C.-H. Yang, A. Rossi, M. F. Gonzalez-Zalba, F. Hudson, A. Morello, and D. J. Reilly *et al.*, Gate-based single-shot readout of spins in silicon, Nat. Nanotechnol. **14**, 437 (2019).

[54] A. Bienfait, J. J. Pla, Y. Kubo, M. Stern, X. Zhou, C. C. Lo, C. D. Weis, T. Schenkel, M. L. W. Thewalt, D. Vion, D. Esteve, B. Julsgaard, K. Mølmer, J. J. L. Morton, and P. Bertet, Reaching the quantum limit of sensitivity in electron spin resonance, Nat. Nanotechnol. **11**, 253 (2016).

[55] C. Eichler, A. J. Sigillito, S. A. Lyon, and J. R. Petta, Electron Spin Resonance at the Level of 10000 Spins Using Low Impedance Superconducting Resonators, Phys. Rev. Lett. **118**, 037701 (2017).

[56] B. A. Mazin, Superconducting materials for microwave kinetic inductance detectors, arXiv preprint arXiv:2004.14576 (2020).

[57] T. Roy, S. Kundu, M. Chand, A. M. Vadiraj, A. Ranadive, N. Nehra, M. P. Patankar, J. Aumentado, A. A. Clerk, and R. Vijay, Broadband parametric amplification with impedance engineering: Beyond the gain-bandwidth product, Appl. Phys. Lett. **107**, 262601 (2015).

[58] D. M. Pozar, *Microwave Engineering* (Wiley, Hoboken, NJ, 2012), 4th ed., oCLC: ocn714728044.

[59] J. Ulrich and F. Hassler, Dual approach to circuit quantization using loop charges, Phys. Rev. B **94**, 094505 (2016).

[60] B. Yurke and E. Buks, Performance of cavity-parametric amplifiers, employing kerr nonlinearites, in the presence of two-photon loss, J. Lightwave Technol. **24**, 5054 (2006).

[61] S. Boutin, Ph.D. thesis, Université de Sherbrooke, 2015.

[62] C. W. Gardiner and M. J. Collett, Input and output in damped quantum systems: Quantum stochastic differential equations and the master equation, Phys. Rev. A **31**, 3761 (1985).

[63] M. S. Khalil, M. J. A. Stoutimore, F. C. Wellstood, and K. D. Osborn, An analysis method for asymmetric resonator transmission applied to superconducting devices, J. Appl. Phys. **111**, 054510 (2012).

[64] S. Probst, F. B. Song, P. A. Bushev, A. V. Ustinov, and M. Weides, Efficient and robust analysis of complex scattering data under noise in microwave resonators, Rev. Sci. Instrum. **86**, 024706 (2015).

[65] C. M. Wilson, T. Duty, and P. Delsing, in *Fluctuating Nonlinear Oscillators*, edited by M. Dykman (Oxford University Press, 2012), p. 390.

[66] Low noise factory: Lnf-lnc0.3_14a cryogenic low noise amplifier, https://www.lownoisefactory.com/products/cryogenic/03-14a/, accessed: 01/08/2021.

[67] D. F. Walls and G. J. Milburn, *Quantum Optics* (Springer, Berlin, 2008), 2nd ed.

[68] A. Ranadive, M. Esposito, L. Planat, E. Bonet, C. Naud, O. Buisson, W. Guichard, and N. Roch, A reversed kerr traveling wave parametric amplifier, arXiv preprint arXiv:2101.05815 (2021).